Review Article

ADVANCED PHOTONICS

Femtosecond laser-inscribed optical waveguides in dielectric crystals: a concise review and recent advances

Lingqi Li,[a] Weijin Kong,[a] and Feng Chen[b,*]

[a]Qingdao University, College of Physics Science, Center for Marine Observation and Communications, Qingdao, China
[b]Shandong University, School of Physics, State Key Laboratory of Crystal Materials, Jinan, China

Abstract. Femtosecond laser inscription or writing has been recognized as a powerful technique to engineer various materials toward a number of applications. By efficient modification of refractive indices of dielectric crystals, optical waveguides with diverse configurations have been produced by femtosecond laser writing. The waveguiding properties depend not only on the parameters of the laser writing but also on the nature of the crystals. The mode profile tailoring and polarization engineering are realizable by selecting appropriate fabrication conditions. In addition, regardless of the complexity of crystal refractive index changes induced by ultrafast pulses, several three-dimensional geometries have been designed and implemented that are useful for the fabrication of laser-written photonic chips. Some intriguing devices, e.g., waveguide lasers, wavelength converters, and quantum memories, have been made, exhibiting potential for applications in various areas. Our work gives a concise review of the femtosecond laser-inscribed waveguides in dielectric crystals and focuses on the recent advances of this research area, including the fundamentals, fabrication, and selected photonic applications.

Keywords: femtosecond laser writing; femtosecond laser inscription; optical waveguides; dielectric crystals; laser crystals; nonlinear optical crystals; waveguide lasers; frequency/wavelength conversion; quantum photonic chip; quantum memories.

Received Oct. 10, 2021; revised manuscript received Jan. 27, 2022; accepted for publication Feb. 23, 2022; published online Mar. 29, 2022.

[DOI: 10.1117/1.AP.4.2.024002]

1 Introduction

Optical dielectric crystals play crucial roles in a large number of optical and photonic applications.[1–3] For example, crystalline quartz is an ideal material for waveplates to modify the polarization state of light. Nonlinear optical crystals, such as $KTiOPO_4$,[4] β-BBO,[5] or $LiNbO_3$,[6] are used to realize selected wavelength conversion in broadband covering visible to the mid-infrared (MIR). Laser crystals serve as gain media that are capable of emitting coherent laser radiation in various solid-state systems.[7] As an emerging direction of intriguing applications of dielectric crystals, quantum photonic devices are also achievable based on specific crystal materials.[8–15] Regardless of the attractive features of crystals, there is a strong desire to construct on-chip or three-dimensional (3D) devices to implement multifunctions in compact systems.[16–19] In photonics, such devices are based on structures of optical waveguides. The light propagation can be confined in waveguides in a diffraction-free way due to the total internal reflection, in which the optical intensity is able to reach a high level.[20,21] With these advantages, the waveguide-based devices therefore have a compact size, robust functionality, high efficiency, and high-cost effectiveness.[22] Optical waveguides based on crystals are attractive for a variety of applications, owing to the combination of advantages of both waveguiding structures and crystal bulk features.[23,24] Toward this purpose, several techniques have been developed to fabricate waveguides in crystal bulks, including metal–ion indiffusion,[25] ion exchange,[26] optical induction,[27] ion implantation,[28] and femtosecond laser inscription/writing.[29–31] However, due to the diversity of the crystal structures and physical, chemical, or optical properties, some techniques are only applicable to specific materials. Among these solutions, femtosecond laser

*Address all correspondence to Feng Chen, drfchen@sdu.edu.cn

writing has been recognized as an efficient tool to fabricate waveguides in versatile crystals owing to the powerful 3D engineering capability and microscale localized refractive index modification.[23,32] The first scenario of dielectric waveguides was realized in glasses through femtosecond laser writing by Davis et al. in 1996.[33] Since then, quite extensive studies have been performed on this topic, and the materials used have also been extended to single crystals, ceramics, and organic materials.[34–38] Various fabrication techniques of laser-written waveguides and related photonic applications have taken a considerable leap forward in the past two decades. For example, using structured light writing, the production of complex waveguides can be implemented in single-way scanning.[39,40] The beam shaping of femtosecond laser pulses can form tracks along selected orientations inside the dielectrics.[41,42] In addition to well-developed waveguide lasers[7] and wavelength converters,[43] emerging applications in quantum photonics have been realized in laser-written waveguides, such as quantum chips[44–49] and memories.[50–53] There are several reviews demonstrating the research progress of the topic from different perspectives;[9,23,24,31,34,35,37,54] however, since this is a hot topic with rapid development of technical solutions and applications, a timely concise review of the new results obtained in recent years on selected branches is desired, particularly on femtosecond laser-written crystal waveguides. In this work, we concentrate on the crystalline waveguides on the newly developed femtosecond laser inscription techniques, the diverse waveguide geometries, the engineering of waveguide modes, and selected applications by presenting an overview of the recent advances in this topic.

2 Modification Induced by Femtosecond Laser Processing of Dielectric Crystals

Focused femtosecond laser beams attain very high optical intensities. As such intense ultrafast beams irradiate the dielectrics at the focal plane inside the materials, strong-field ionization (multiphoton or tunnel ionization) occurs,[55,56] which makes a large number of electrons break away from their original atoms. These free electrons continue interacting with the laser pulse, and more electrons are released by collisions, leading to avalanche ionization.[57] Consequently, a hot and dense electronic plasma forms.[58] If the free electrons reach a value close to the plasma density for the laser wavelength, breakdown occurs, resulting in ablation at the surface and fissures in the bulk,[59] modifying the irradiated lattices significantly. Since the interaction process happens on an ultrashort timescale, the thermal implication to the surrounding region of the focus can be very limited, particularly in regimes of low-repetition-rate pulses,[60] depending on the hot electrons coupling to the lattice and the heat relaxation, but can also modify the bulk properties.[61,62] As a result, the femtosecond laser modification of the dielectrics is very localized, which enables "cold" micromachining of materials. The femtosecond laser modification may bring out some effects in dielectrics, such as refractive index changes,[33] stress,[63] birefringence,[64] nanogratings,[65,66] voids,[67,68] and thermal melting.[69] To promote permanent refractive index changes in the focal volumes, which are the base for waveguides, the pulse intensity has to be carefully controlled to avoid breakdown.[70,71] Nevertheless, the processes of femtosecond laser modification are generally very complex and strongly rely on the nature of materials and parameters of laser pulses. The major parameters of laser pulses include wavelength,[72] energy,[73] repetition rate,[74] focusing condition, scanning speed, and/or polarization.[75] Generally, for a specific material, it is required to be transparent at the selected laser wavelength, i.e., the linear optical absorption of the material at the used laser wavelength is minimal. Because the femtosecond laser relies on a nonlinear optical process, the strong linear absorption may bring out incubation effects and significant thermal effects (e.g., ablation at large-scale regions), which lead to modifications staring at the surface, preventing bulk machining.[76] For example, near-infrared lasers at 800 nm or 1 μm are used to process most insulating dielectrics, while for silicon the 1.5-μm laser works well for waveguide inscription.[77] In addition, waveguides have been successfully produced by green-laser writing in dielectrics with negligible absorption at the visible light band.[78–80] In addition, low-repetition-rate (~kHz) lasers deposit less energy onto the lattice per unit length of the samples, which requires the relatively high energy of single pulses.[74,81] High-repetition-rate (MHz) pulses induce thermal effects, and are often used for glass waveguide fabrication.[82]

2.1 Type I and Type II Modifications

For dielectric crystals, waveguide formation depends on the efficient modification of the refractive index of the bulk. There are two major effects of refractive index changes, i.e., types I and II.[63] Type I refers to the laser-induced tracks with positive index changes ($\Delta n > 0$) that may be due to the slight structural change of lattices. Such variation may be correlated to the breaking of the symmetry of the irradiated lattices.[83–85] To form type I modification, low-energy pulses are required. Recent investigation reveals that the type I modification may also be due to the phase transition of the laser-irradiated regions.[86,87] Type II refers to laser created filaments in the material, which has negative index changes ($\Delta n < 0$) caused by localized crystalline lattice expansion in the focal volume.[63] The type II modification is typically correlated to highly altered lattices in which partial or complete amorphization occurs. For type I modifications, the track region is able to guide light because it has a higher refractive index than the surroundings, whereas for type II, the track has a lower index and cannot be used as a waveguide; however, the expansion of volume in the focal plane gives rise to compression of vicinity, leading to the refractive index increments in the surrounding of the track.[60] With these typical features, several configurations of waveguides have been developed based on types I and II modifications. Figure 1 shows the typical geometries of four basic laser-written waveguides: single-line, double-line, depressed-cladding, and optical-lattice-like structures. For $\Delta n > 0$ in the track, the single-line can be used to guide light since it naturally constructs a waveguide channel [Fig. 1(a)], and such structures are easy for 3D waveguide fabrication.[88,89] However, in crystals, the single-line structure is usually polarization sensitive[84,85] and does not possess good thermal stability.[32] Another disadvantage is that the waveguide core lattice has been distorted by the laser irradiation and, for crystals, the bulk features are destroyed in the waveguide.[90] Based on type I modification, a multiscan technique can be employed for the fabrication of symmetrical waveguides in which several single-line tracks are overlapped transversal to the writing direction.[91] Such a design is preferred to support waveguiding accessible to long wavelengths with low-loss propagation owing to a significant increase of the index contrast.[89] For $\Delta n < 0$, the track region has a low index in comparison with

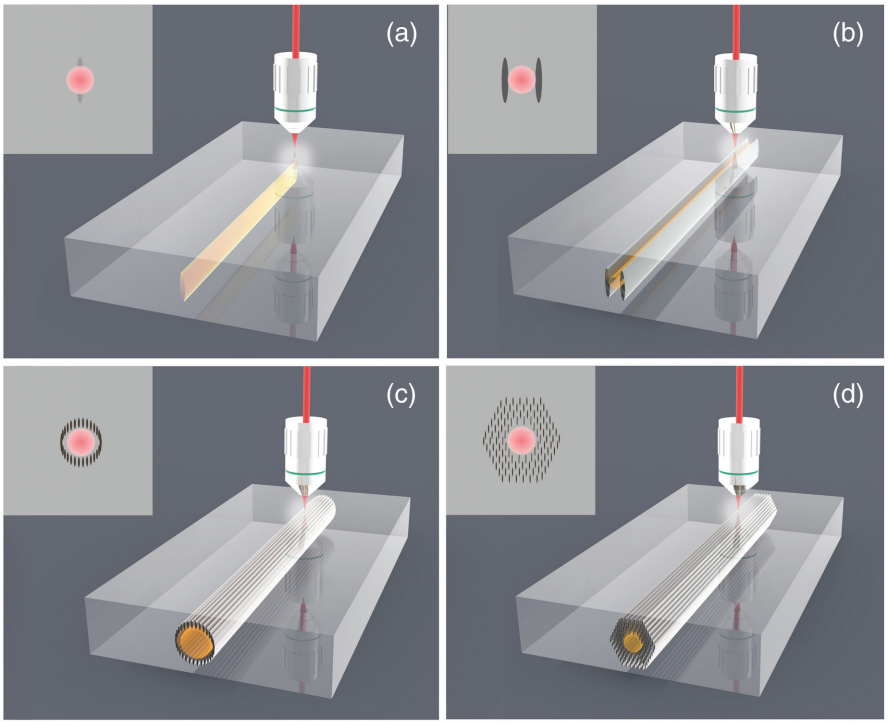

Fig. 1 Basic geometries of laser writing of waveguides: (a) single-line, (b) double-line, (c) depressed-cladding, and (d) optical-lattice-like configurations. The dark (gray) regions represent the laser-induced tracks.

the surrounds, and the vicinal zones have a relatively high index that may serve as guiding regions.[92] In practice, to obtain a nearly symmetric waveguide core, the double-line structure is used: the guiding core is located at the region between two parallel tracks [Fig. 1(b)]. The waveguide core is not located at the tracks that have highly altered lattices. This means that the properties of the bulk crystals are well-preserved in the waveguides[93,94] in which the laser-induced modifications of the original lattices are negligible.[95] In addition, the formed track has excellent thermal stability, enabling applications under high-power conditions.[96] There are shortcomings offered by the double-line waveguides, which cannot guide light at longer wavelengths since the dimension of the waveguide core is limited to <20 μm, and for 3D fabrication it requires a complicated design.[97] The depressed-cladding structure is a more flexible solution [Fig. 1(c)]. It is usually in the geometry of circles or rectangles,[98] which consists of a number of type II tracks. Since the diameters of cladding waveguides can be artificially determined, they are capable of guiding long-wavelength light, e.g., MIR regime.[78,80,99] Nevertheless, for 3D waveguides, it also requires a special design. A special configuration is an "optical-lattice-like" structure,[100] which contains a periodically arranged array of tracks [Fig. 1(d)]. Some positions are free of any tracks, e.g., in the center of the structure, which can serve as beam propagation channels. By modulating the geometries of tracks, it is able to achieve beam transformation and shaping.[101,102] Generally, the maximum Δn of type I modification is much lower than that of the type II modification induced by femtosecond laser irradiation.[32] For instance, the typical index variation of type I waveguides in $LiNbO_3$ crystal does not go beyond 1×10^{-3}, whereas this value will increase to (2 to 5) $\times 10^{-3}$ at directly irradiated tracks for type II-based structures.[23,63] For Nd:YAG double-line waveguides, Δn as high as 9×10^{-2} at type II filaments has been determined according to μ-Raman and μ-photoluminescence microscopic analysis.[92] Most recently, quantitative phase microscopy became a popular method to recover the index contrast of the waveguides from the phase image. In particular, the index change of 2.5×10^{-3} has been maintained after heating up to 1400°C for a depressed cladding waveguide inscribed in a sapphire crystal that exhibited 4.75×10^{-3} prior to the annealing process.[80] Table 1 summarizes the advantages and disadvantages of different configurations in transparent solid materials (crystal, glass, polymer, ceramic, etc).

One could realize the evolution of laser-written tracks from type I to type II via manipulating the laser inscription parameters. For instance, in $LiTaO_3$ crystal, with the low-repetition rate of femtosecond laser pulses (25 kHz), the tracks can be changed from type I to type II. Figure 2(a) shows the influence of incident pulse energy on the geometry of tracks at a fixed laser scanning speed. With the increase of pulse energy, the type I region gradually moves down along the direction that the laser propagates and an elongated filamentation with type II modification appears. This can be explained by the competition of self-focusing and plasma defocusing when the peak power is higher than the critical power P_{cr}:[32]

$$P_{cr} = \frac{3.77\lambda^2}{8\pi n_0 n_2}, \tag{1}$$

where λ is the wavelength, n_0 is the linear refractive index, and n_2 is the nonlinear refractive index. In addition, the laser scanning velocity can be changed to obtain different types of tracks. Figure 2(b) represents the microscope images of laser-written

Table 1 Advantages and disadvantages of different configurations in transparent material.

Waveguide configuration	Advantages	Disadvantages
Type I	1. Direct writing for 3D micromachining 2. Single-mode guiding structures 3. Longer wavelength guidance using multiscan technique	1. Distorted lattices with degraded bulk features 2. Bad thermal stabilities 3. Guidance only along one polarization 4. Realizable in limited crystals
Double line	1. Well-preserved bulk features 2. Single- or low-order mode structures 3. Being easily achieved in crystals 4. Excellent thermal stabilities 5. Wide applicability in crystals	1. No guidance at long wavelength (e.g., mid-IR) 2. Guidance only along one polarization in some crystals (e.g., cubic YAG) 3. Being difficult for 3D waveguides
Depressed cladding	1. Well-preserved bulk features 2. Guidance till long wavelength 3. Designed geometry and adjustable diameters 4. Very good thermal stabilities 5. High coupling efficiency with fibers 6. Potential guidance along any transverse direction 7. Wide applicability in crystals	1. Relatively longer production time 2. Being difficult for 3D waveguides
Optical-lattice-like cladding	1. Being similar to double line and depressed cladding 2. 3D device by special designs	1. Special design for different functions and materials

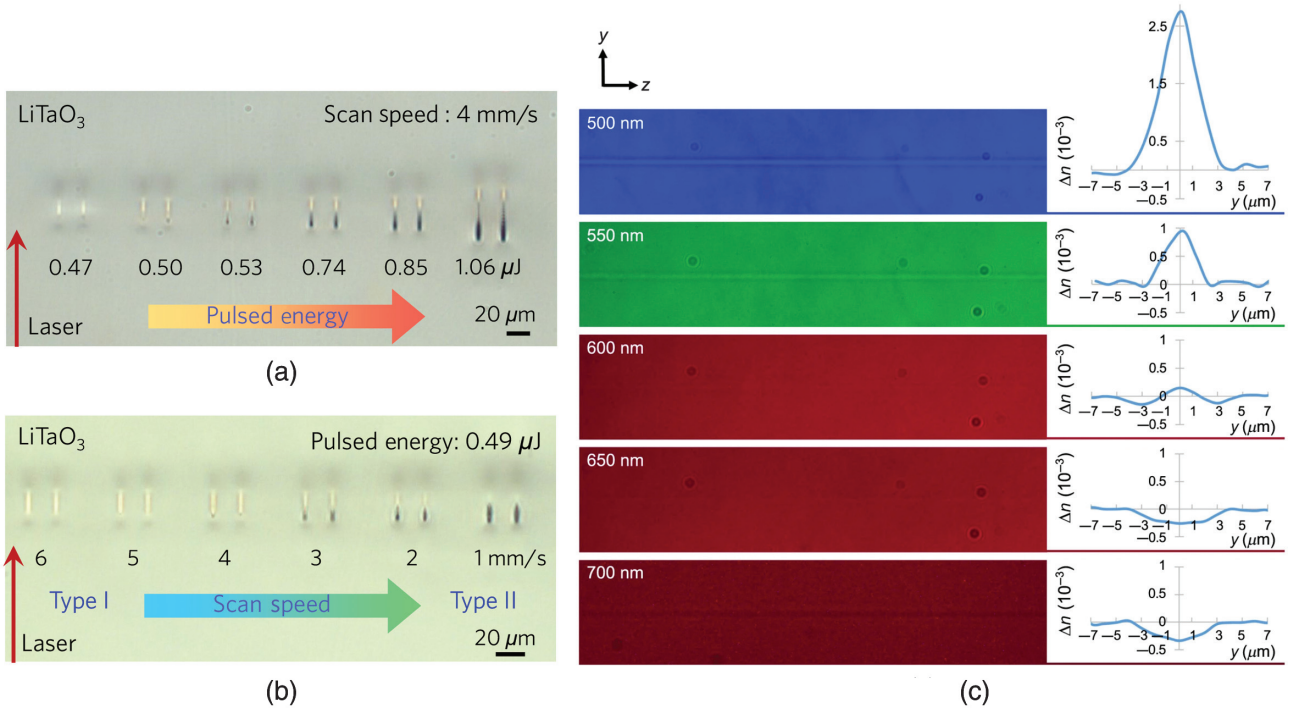

Fig. 2 Optical microscope images of laser-induced tracks with (a) different pulse energies and (b) scanning velocity in $LiTaO_3$ crystal. (c) Different refractive index change profiles from positive to negative, depending on the propagation wavelength in ZnSe crystal. Image (c) is reproduced with permission from Ref. 103, Creative Commons Attribution License (CC-BY).

tracks modified from type I to type II, as the scanning speed changes from 6 to 1 mm/s, whereas the pulse energy keeps a fixed value of 0.49 μJ. As the scanning speed decreases, more energy is deposited in the crystal unit volume, leading to more severe lattice distortion or damage, therefore, the slight type I modification will evolve into type II modification. More than that a new phenomenon allowing a significant increase of the refractive index contrast has been recently reported, which is called the effect of femtosecond-laser-induced electronic bandgap shift (FLIBGS).[103] When FLIBGS occurs, the absorption edge of the transmission spectrum shifts. At a propagation wavelength near the transparent material electronic resonance, the FLIBGS greatly affects the absorption and thus the refractive index, as predicted by the Kramers–Kronig relations.[104] By employing the effect of the FLIBGS, the tracks created by the femtosecond laser exhibit a dispersion of the refractive index, which in ZnSe crystals is the signal of the variation from positive to negative, as shown in Fig. 2(c). However, the FLIBGS effect generally happens in a narrow wavelength window. According to Lapointe et al.,[103] at a specific propagating wavelength, the refractive index modification becomes zero ($\Delta n = 0$), which means the laser inscription should be invisible, paving the way for new invisibility applications.

2.2 Control of Laser-Induced Tracks

The track morphology is crucial for laser inscribed waveguides because the track geometry plays an important role in the refractive index changes and stress fields. In addition, track engineering is also essential for nonlinear domain modification and well-defined microstructures.

2.2.1 Effect of writing parameters

For a given laser writing system, the main parameter that determines the localized modification in focal volume is the pulse intensity (or fluence).[32] At low pulse intensity but beyond the optical modification threshold, an isotropic refractive index change is achieved,[105] whereas a birefringent refractive index change has been obtained at intermediate intensity.[106] Higher pulse intensity will lead to empty voids caused by microexplosions,[107] depending on the properties of the material. The transverse intensity distribution of the laser beam could be written as[108]

$$I(r,z) = \left(\frac{w_0}{w(z)}\right)^2 \exp\left(-\frac{2r^2}{w^2(z)}\right), \tag{2}$$

where r is the radial distance and z is the axial distance from the beam waist. $w(z)$ is the variation of the laser beam spot size (the distance from the beam axis where the intensity drops to $1/e^2$ of the maximum value) and is given by

$$w(z) = w_0\sqrt{1+\left(\frac{z}{z_0}\right)^2}, \tag{3}$$

and w_0 is the diffraction-limited minimum beam waist radius:

$$w_0 = \frac{M^2\lambda}{\pi \mathrm{NA}}, \tag{4}$$

where M^2 is the Gaussian beam quality factor and NA is the numerical aperture of the focusing objective. The Rayleigh range of the focus within a transparent material having a refractive index n is given by

$$z_0 = \frac{M^2 n\lambda}{\pi \mathrm{NA}^2}. \tag{5}$$

The laser beam focus size at the focal plane is simply given by the w_0 and z_0 in the transverse and axial directions of the incident beam when neglecting optical aberrations and nonlinear effects. The peak intensities reached at the focal volume of the transparent material are:

$$I_p = \frac{E_p}{\pi w_0^2 \tau_p}, \tag{6}$$

where E_p is the pulse energy and τ_p is the pulse duration. As we can see, the beam waist determines the transversal size of the modifications induced in the dielectrics; together with the scanning velocity, they define the pulses superposition and the total amount of the energy delivered at a focal spot. It also defines the pulses that have enough intensity to promote changes in the material.

Generally, the higher the energy of laser pulses is, the more modified the tracks are.[90] In addition, higher-speed scanning creates weaker tracks.[23] This is easily understandable because the track geometry is determined by the average energy deposition of the unit volume in the samples. Figure 3(a) shows the laser-induced tracks in a Nd:YVO_4 crystal at different energies and scanning rates (the repetition rate of the laser is set at 1 kHz). Similar effects are observed for other crystals. Therefore, the choice of energy and scanning rate for a successful waveguide fabrication is to balance both effects on dielectric materials. The energy of pulses is typical of micro-Joule (μJ) or sub-μJ, and the used scanning rate ranges from tens of μm/s to tens of mm/s. The polarization of femtosecond laser pulses may also affect the track writing, although in most cases, the effect is negligible. For example, in an optical-lattice-like structure of Nd:YAP crystal,[75] as femtosecond laser polarization is perpendicular to the scan direction, the waveguide cores are located in the regions between adjacent tracks, while in the center of the structure in the case of polarization parallel to the scan orientation. Figure 3(b) shows the optical microscope image of the lattice-like structure in a Nd:YAP crystal and the guided modes obtained under different laser polarizations.

2.2.2 Properties of crystal materials

The unique characteristics of crystal materials, such as birefringence and optical nonlinearities will affect the track morphology. For example, in Nd:$GdVO_4$, along the crystalline orientation of the c axis, the incident laser is split into two beams inside the crystal due to the high birefringence; as a result, two tracks are created at one shot of a single-laser pulse [Fig. 3(c)]. Nevertheless, such behaviors strongly depend on the used laser parameters and the bulk features. In many cases, nonlinear optical effects highly influence the propagation of femtosecond laser pulses in crystals, resulting in the morphology of tracks that are more likely to be an elongated filamentation or structure with multifoci not only a single focus.[110,111] It is a very complex dynamic process. As the light propagates through a dielectric, the optical response is described as a macroscopic polarization induced by displacement of bound charges. For the simplified case of a centrosymmetric material that nullified the second order

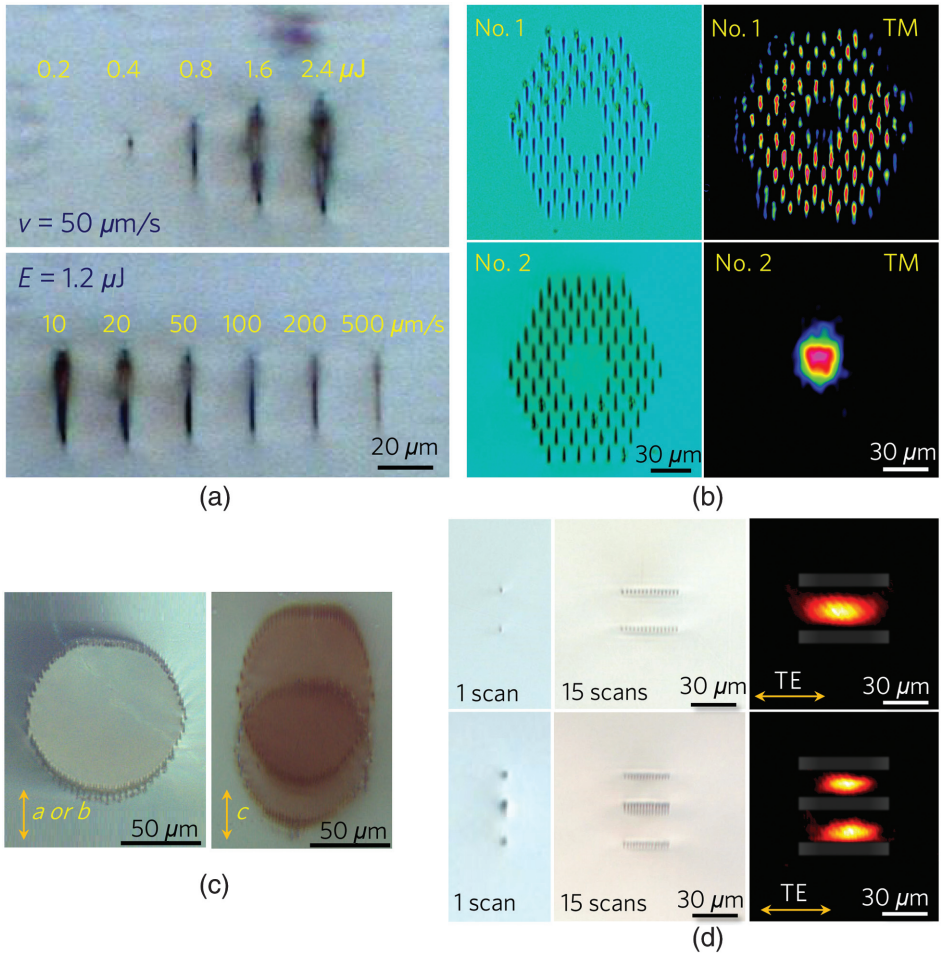

Fig. 3 (a) Microscope images of tracks with different pulse energies and scanning rates in Nd:YVO_4. (b) Influence of different laser polarizations on the tracks and modal profiles in Nd:YAP, perpendicular to the scans (No. 1) and parallel to the scans (No. 2), respectively. Images reprinted from Ref. 75, © 2016 The Optical Society (OSA). (c) Optical images of tracks as the laser writing along different crystalline orientations in Nd:$GdVO_4$. (d) Laser-induced multifoci in $LiTaO_3$, corresponding horizontal waveguides, and modal profiles. Reprinted with permission from Ref. 109, © 2019 IEEE.

(an all even order), if fourth and higher order nonlinear effects are neglected, the polarization of a centrosymmetric medium can be written as[112]

$$\mathbf{P}(t) = \varepsilon_0\left(\chi^{(1)} + \frac{3}{4}\chi^{(3)}|\mathbf{E}|^2\right)\mathbf{E}(t), \tag{7}$$

where $\chi^{(i)}$ is the ith order nonlinear susceptibility and $\mathbf{E}(t)$ is the incident electric field. The refractive index of the material is defined by n_0 and n_2 (optical Kerr effect) when the linear part dominates over the nonlinear part:[32]

$$n = \sqrt{1 + \chi^{(1)} + \frac{3}{4}\chi^{(3)}|\mathbf{E}|^2} = n_0 + n_2 I, \tag{8}$$

where $n_0 = \sqrt{1+\chi^{(1)}}$, $n_2 = \frac{3}{4}\frac{\chi^{(3)}}{\varepsilon_0 c n_0^2}$, and $I = \frac{1}{2}\varepsilon_0 n_0 c|\mathbf{E}|^2$ is the laser intensity. Thereby, a spatially dependent intensity of the Gaussian laser beam modifies the effective refractive index of dielectrics. In most media, the n_2 is positive and the refractive index at the center of the beam is higher than in the wings, acting as a positive lens to self-focus the light, as if the femtosecond laser pulse exceeds the P_{cr}, a collapse occurs at a focal point. Additionally, the convex effect induces sufficient intensity to create ionization and other nonlinear effects, forming an electron plasma that acts as a concave lens to defocus the laser beam. The self-focusing comes again provided the intensity is higher than the P_{cr}. Such a spontaneous multiple focusing can be realized in both type I and type II regimes. For example, in $LiNbO_3$ crystals, under the high-repetition-rate of femtosecond laser (700 kHz) for type II modification, the altered track consists of three point-like structures at a single shot, which is identified with a periodic distribution of lattice defects.[113] Furthermore, the laser-induced grating structure of a period ~1.2 μm is also implemented. In addition, in the regime of low repetition rate (8 kHz), the multifoci tracks based on type I modification can be demonstrated as the energy increases and the track morphology is determined by the energy of laser pulses.[91] Another interesting sample is $LiTaO_3$ crystal, where the multiple-focusing

spots with different numbers are also realized, depending on the laser-irradiated parameters.[109] Using the multiscan technique, researchers have fabricated desired structures to obtain horizontal tracks for waveguide-guiding along with TE polarization, whereas the normal double-line waveguide only supports TM polarization [Fig. 3(d)]. In this design, the layer of the waveguide is composed of a number of modified points, forming a dotted line, and the total length can be controlled by the laser scans. Theoretically, more layers of waveguides can be possibly obtained using this approach.

2.2.3 Beam shaping techniques

During the process of femtosecond laser irradiation, the laser beam is generally fixed and focused at a certain depth beneath the sample surface. The sample is usually mounted on a computer-controlled *XYZ* linear stage to realize an arbitrary shape, and a CCD system is used to monitor the waveguide writing process. The sample can be translated along the beam propagation direction, i.e., longitudinal writing, or orthogonally to, i.e., transverse writing.[60] The waveguide formed by longitudinal writing has intrinsic circular symmetry, while it is restricted by the working distance of the objective lens and it has limitations in 3D layouts.[114] In contrast, the design flexibility of transverse writing is enormous and allows for the fabrication of 3D structures,[23,60] in spite of their asymmetric cross sections.

Over the past decades, beam-engineering techniques have been developed to improve the shape of the laser-written waveguides, such as the double-beam technique,[115] adding cylindrical lenses,[116] the slit technique,[41] using a nondiffractive Bessel beam,[117] and using a spatial light modulator (SLM).[39] Figure 4(a) illustrates the writing process of depressed cladding waveguides utilizing an ellipsoidal focal spot, where a number of tracks are inscribed one by one, thus, resulting in a time-consuming process. Nowadays, SLMs have been used widely in femtosecond laser processing. From the work of Qi et al., the fabrication times have been considerably reduced,[41] as shown in Fig. 4(b). The phase mask for writing horizontal lines is presented in Fig. 4(c). Thereby, horizontal tracks can be employed to construct the

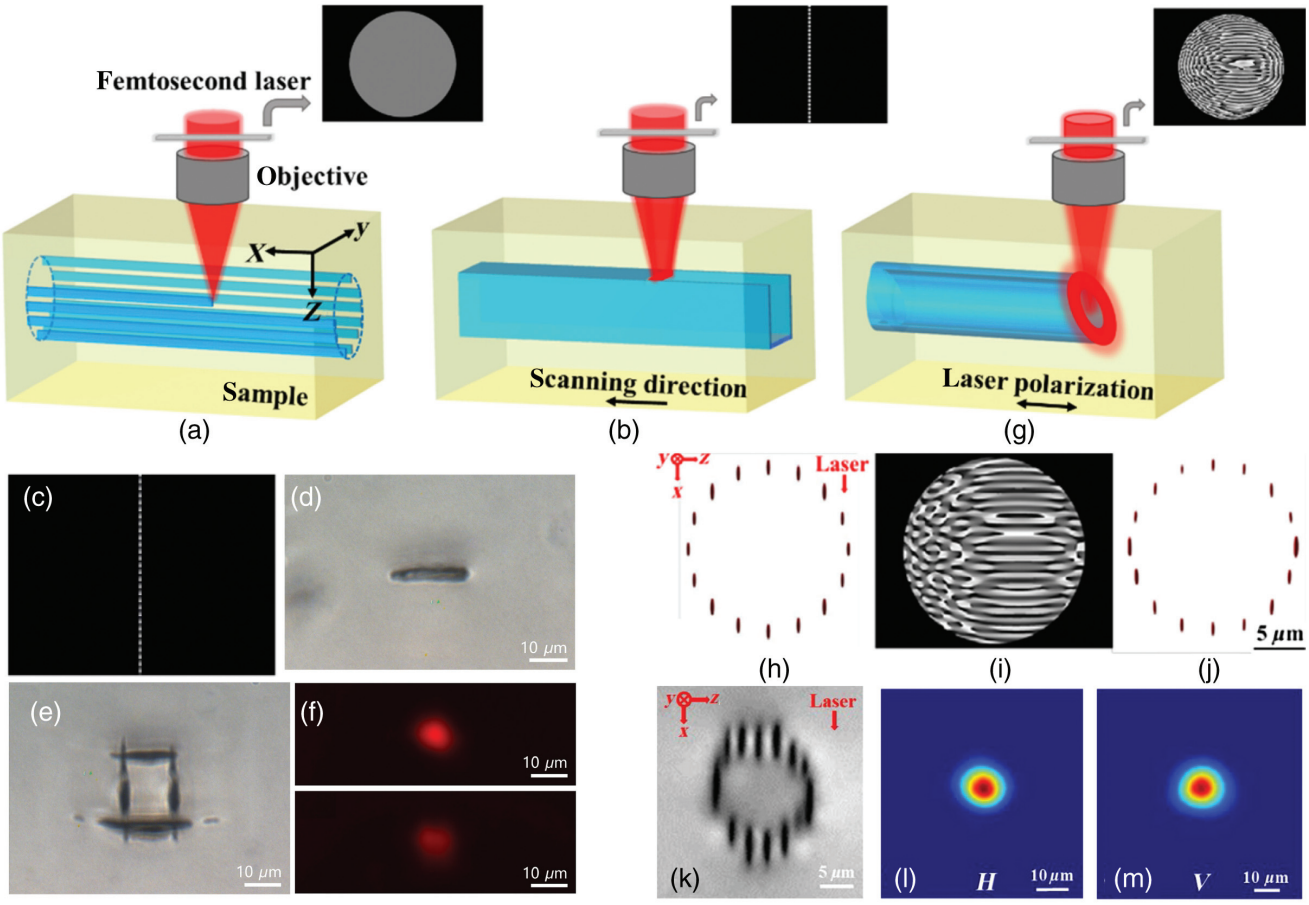

Fig. 4 Schematic diagram of direct laser-written cladding waveguides (a) with an ellipsoidal focal spot and (b) with a slit-shaped beam focus. Images (a), (b), and (g) are reprinted with permission from Ref. 40, © 2017 OSA. (c) The phase mask for writing horizontal lines. Microscope image of (d) horizontal tracks, (e) waveguide, and (f) near-field profiles. Images (c)–(f) are reproduced with permission from Ref. 42, CC-BY. (g) Schematic plot of single-scan cladding waveguides utilizing a longitudinal ring-shaped focal field. (h) Calculated 3D isosurface, (i) phase mask, and (j) simulated focal intensity profile. (k) Microscope image and (l), (m) corresponding modal profiles. Images (h)–(m) are reprinted with permission from Ref. 118, © 2019 Chinese Laser Press (CLP).

cladding of waveguides in a $LiNbO_3$ crystal that exhibit the polarization-independent guidance[42] [Figs. 4(d)–4(f)]. Later in 2019, Zhang et al.[118] proposed a single-scan method to fabricate cladding waveguides using 3D engineered focal field [Figs. 4(g)–4(j)]. The longitudinally oriented ring-shaped focal field is composed of 16 discrete spots, allowing for the generation of annular cladding waveguides at a single shot of laser writing, demonstrated in Figs. 4(k)–4(m). Most recently, Sun et al.[39] developed a new and efficient multifoci-shaped femtosecond pulsed method to write circular symmetric waveguides with an SLM.

2.2.4 Nonlinear domain engineering

The morphology of tracks is crucial for not only waveguide configuration but also for engineering the crystal properties to achieve modulation of nonlinearity polarization. Especially for type II modification, focused laser pulses will cause highly damaged lattices, where an amorphous volume forms that reduces the nonlinear coefficient. Such a modification can be periodically introduced to realize spatial modulation of the second-order nonlinear coefficient $\chi^{(2)}$, enabling quasi-phase-matching (QPM) structures,[119] also known as nonlinear photonic crystals (NPC).[120] Thereby, the researchers have fabricated 3D NPCs by selectively erasing the nonlinear coefficients of a $LiNbO_3$ crystal.[121] The recently developed 3D NPCs present efficient generations of second-harmonic vortex and Hermite–Gaussian beams, showing the potential for nonlinear beam-shaping devices[6] and nonlinear volume holography[122,123] in comparison to the two-dimensional (2D) case. Additionally, the huge flexibility of direct laser writing enables complex 3D domain structures,[43,120] allowing their monolithic integration with other phase modulators and switches, and improving the performances and functions of on-chip devices. Using the same strategy of domain erasing in a quartz crystal, researchers from Shandong University have realized tunable second harmonic generation (SHG) down to the ultraviolet wavelength.[124] In addition, there will be an obvious thermal effect at the high-repetition rate of femtosecond laser pulses, which can be utilized to realize reversed polarization. The group from Australia reported on the similar 3D domain structures in a BCT crystal by femtosecond laser direct writing through the thermoelectric-field poling,[125] allowing for precise domain inversion with high resolution. This laser engineering strategy can be extended to other systems of crystals.

Moreover, laser-induced quasi-phase-matching (LiQPM) grating structures inside the waveguide's core allow efficient frequency conversion, which opens new avenues for advanced all-integrated nonlinear devices. For instance, using femtosecond laser-induced domain inversion in $LiNbO_3$ waveguides, a conversion efficiency of 17.45% for frequency doubling of 815 nm has been demonstrated.[126] In addition, a depressed cladding waveguide-integrated LiQPM grating scheme has been proposed by Denz et al.[127] With the precise and flexible 3D domain engineering, as shown in Figs. 5(a) and 5(b), they have realized broadband and multiwavelength frequency conversions.[43] Particularly, the second harmonic vortex can be demonstrated by a helical twisted domain grating into a waveguide, as depicted in Figs. 5(c)–5(e).

2.2.5 Well-defined micro- and nanostructures

The laser-written track is also promising for creating spatially well-defined microstructures in combination with chemical wet etching. In the laser-modified volumes, the femtosecond pulses have driven the crystal network to a predamaged state that shows a larger selective etching than the unperturbed bulk lattices.[128] A good sample is the YAG crystal, as shown in Fig. 6(a), where the optical-lattice-like waveguide is fabricated by direct laser writing, and then the sample is immersed into the selected acid (e.g., phosphoric acid).[129] As one can see, after some time,

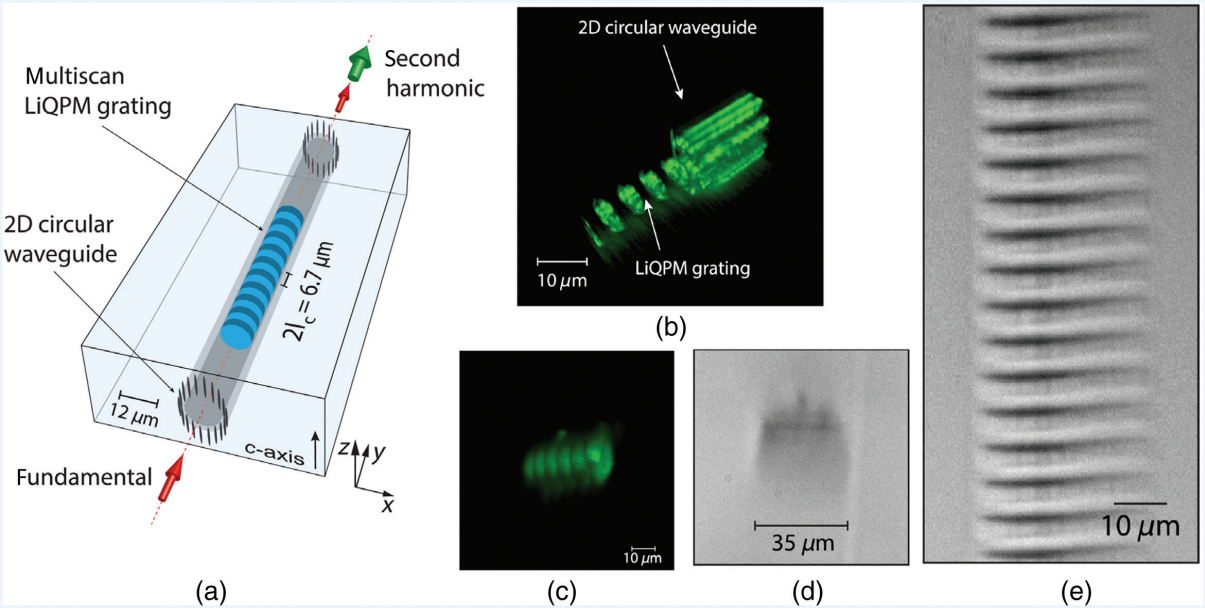

Fig. 5 (a) Schematic design of a waveguide-integrated LiQPM grating; (b) SH microscope image of LiQPM grating and waveguide; and (c) helical grating structure. Microscope image of the helical structure: (d) the front face and (e) top view. Images reprinted with permission from Ref. 43, © 2020 OSA.

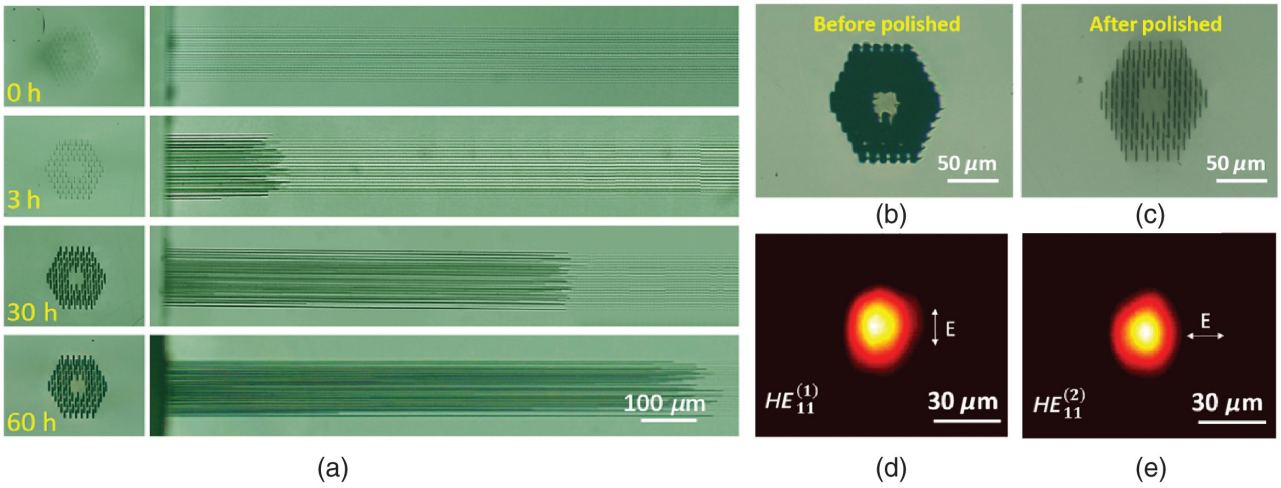

Fig. 6 (a) Microscope images of hollow optical-lattice-like structures at different etching times in YAG crystal. (b) Before polished and (c) after polished. Near-field modal profiles at 4 μm along (d) TM and (e) TE polarization, respectively. Images reproduced with permission from Ref. 129, © 2020 CLP.

the etched portion of the damaged track is filled with air, thus resulting in a larger refractive index change than the unetched region [Figs. 6(b) and 6(c)]. Therefore, the confinement of the light field will be enhanced. In this work, the etched microstructured optical waveguide supports good guidance at the MIR wavelength of 4 μm [Figs. 6(d) and 6(e)], which is impossible for structure before etching. Actually, early in 2013, Kar et al. produced large microfluidic channels within YAG by selectively wet etching laser-written type I tracks.[130] The technique is very interesting and offers an efficient solution to 3D nanolithography of crystals. In 2019, Osellame et al.[131] reported on the nanopores with mm-scale length. By implementing auxiliary vertical etching pores to build a 3D-connecting etching architecture, they have achieved 3D nanolithography with a long length. Using this strategy, they have produced subwavelength diffraction gratings and microstructured waveguides in YAG crystals.

2.3 Mode Guidance Correlated to Crystal Systems

Dielectric crystals are important media for optical and photonic applications, which can be roughly cast into a few groups, such as laser crystals, nonlinear optical crystals, and electrooptic crystals.[23] Unlike the amorphous substrates, crystalline material entails structures of long-range orders of lattices, offering unique physical properties that are not exhibited in glass, such as even order optical nonlinearities and birefringence.[1] There are seven crystal systems to characterize the crystal lattices or structures of different geometries, i.e., cubic, tetragonal, hexagonal, trigonal, orthorhombic, monoclinic, and triclinic. Up to the current date, a wide range of crystals has been used for the fabrication of direct laser-written waveguides; for example, YAG crystal belongs to the cubic, $LiNbO_3$, β-BBO, and sapphire crystals belong to the trigonal, and 6H-SiC crystal belongs to the hexagonal crystal family. To some extent, the symmetry of each lattice determines the waveguide properties, such as polarization dependence and propagation loss. Table 2 summarizes the waveguide configurations and guiding properties of typical crystals in different crystal systems. For each lattice family, a brief overview will be given below.

For cubic systems, YAG is one of the most well-studied crystals in the direct laser writing of waveguides. For the depressed-cladding and optical-lattice-like waveguides, symmetric guidance for any polarization, i.e., both transverse magnetic (TM) and electric (TE) are supported,[100,132] whereas the dual-line geometry only allows TM-polarized guidance,[79] which is mainly related to the high symmetry of the cubic system that possesses three fourfold axes of rotation. The cubic-lattice crystals exposed to laser irradiation undergo a severe modification that results in a positive index change in a specific polarization. A similar polarization-dependent guiding behavior is also found in Nd:GGG crystal,[134] another typical cubic crystal. Although for the tetragonal system, such as $Nd:YVO_4$ and $Nd:GdVO_4$, only one fourfold axis of rotation is contained, leading to a lower symmetry than that of the cubic system. As a result, the dual-line structure supports guidance along both TE and TM polarizations[138,141] but is still of slightly anisotropic guidance. The depressed-cladding waveguides in the tetragonal is guided in an anisotropic way as well, which is different from the cubic YAG crystal. As for the hexagonal system, up to now, only 6H-SiC crystal is employed for laser writing of waveguides.[143] Like the cubic system, both TM and TE guidances are determined in rectangular cladding waveguides, whereas only TM guiding mode is supported in dual-line structure. In hexagonal system, there is one six-fold axis of rotation, thus the symmetry is between the cubic and tetragonal systems.

$LiNbO_3$, $LiTaO_3$, β-BBO, and sapphire, as the typical crystals belonging to the trigonal system, exhibit unique nonlinearities and birefringence. Therefore, as these crystals are processed under laser writing, there will be some different structural modifications due to the high-order threefold axis of rotation. Various configurations have been inscribed in $LiNbO_3$ crystal by femtosecond lasers, such as type I modified single-line and multiline structures, type II modified dual-line waveguides, depressed-cladding, optical-lattice-like, and ride waveguides. Generally, in $LiNbO_3$ and $LiTaO_3$ crystals, type I and type II waveguides would suffer from serious polarization-dependent guiding, which only permits polarization along the orientation parallel to the laser-induced tracks,[91,147] whereas

Table 2 Summary of latest published works about waveguide configuration and properties of typical crystals in different crystal systems.

			Guiding properties		
Crystal system	Material	Waveguide configuration	Polarization dependence	Minimum propagation loss (dB/cm)	Ref.
Cubic crystals	Nd:YAG	Type I (single line)	TE and TM	5@632.8 nm	87
		Dual line	TM	0.21@632.8 nm	79
		Double cladding	TE and TM	1.3@632.8 nm	132
		Optical-lattice like	TE and TM	0.7@1064 nm	100
		Cladding + dual line	TE and TM	—	133
	Nd:GGG	Dual line	TM	2.0@632.8 nm	134
		Depressed cladding	TE and TM	1.7@632.8 nm	135
	BGO	Type I (multiscan)	TE and TM	3.22@4 μm	89
		Type I (ring shaped)	TE and TM	1.56@1550 nm	136
		Dual line	TE and TM	0.5/632.8 nm	137
		Depressed cladding	TE and TM	2.1@632.8 nm	137
Tetragonal crystals	Nd:YVO_4	Dual line	TE and TM	0.8@632.8 nm	138
		Depressed cladding	TE and TM	1.1@632.9 nm	139
		Optical-lattice like	—	—	140
	Nd:$GdVO_4$	Dual line	TM	0.5@1064 nm	141
		Depressed cladding	TE and TM	0.7@632.8 nm	142
Hexagonal crystals	6H-SiC	Dual line	TM	0.78@1064 nm	143
		Rectangular cladding	TE and TM	1.62@1064 nm	143
Trigonal crystals	$LiNbO_3$	Type I (single line)	TM	2.22@1064 nm	144
		Type I (multiline)	TM	1.98@632.8 nm	91
		Dual line (vertical)	TM	0.6@1064 nm	63
		Dual line (horizontal)	TE	3.25@1550 nm	41
		Depressed cladding	TE and TM	1.25@1550 nm	118
		Optical-lattice like	TE	1.27@1550 nm	145
		Ridge configuration	TM	3.28@4 μm	146
	$LiTaO_3$	Type I (single line)	TM	2.67@632.8 nm	147
		Dual line (horizontal)	TE	1.7@632.8 nm	109
		Depressed cladding	TE and TM	1.56@1550 nm	148
		Rectangular cladding	TE and TM	0.12@1550 nm	149
	β-BBO	Depressed cladding	TM	0.19@800 nm	150
	Sapphire	Type I	TE and TM	2.3@633 nm	151
		Dual line	TM	0.65@798.5 nm	152
		Depressed cladding	TE and TM	0.37@2850 nm	80
		Optical-lattice like	TE and TM	2.9@1064 nm	153
Orthorhombic crystals	KTP	Type I (multiline)	TM	1.0@980 nm	154
		Dual line	TE and TM	0.8@633 nm	155
		Depressed cladding	TE and TM	1.7@632.8 nm	156
		Optical-lattice like	TE and TM	1.2@632.8 nm	157
	Nd:YAP	Depressed cladding	TE and TM	0.15@1064 nm	158
		Optical-lattice like	TE and TM	1.11@1064 nm	159
Monoclinic crystals	BiB_3O_6	Depressed cladding	TE and TM	0.6@1064 nm	160
	Nd:YCOB	Type I	TM	1,1@1550 nm	85
		Depressed cladding	TM and TE	—	161
	Nd:GdCOB	Double cladding	TM and TE	0.65@633 nm	162
	Nd:KGW	Dual line	TM and TE	2.0@632.8 nm	163
		Depressed cladding	TM and TE	1.8@1064 nm	164

the depressed-cladding waveguide enables isotropic guiding as well as in Ti-sapphire crystal.[165] However, for β-BBO crystal, only TM-polarized guiding is supported in depressed-cladding waveguides.[150] In addition, polarization-dependent guiding also happens in both optical-lattice-like[145] and ridge configurations[146] in a $LiNbO_3$ crystal, which only allows n_0-polarized guidance.

In addition to the crystal system mentioned above there are lower-symmetry crystal families that do not contain a higher-fold axis of rotation, such as orthorhombic system and monoclinic system. In such crystal systems, laser-written waveguides present isotropic guiding behavior. For instance, $KTiOPO_4$ (KTP) is a typical crystal belonging to the orthorhombic system; the guidance for dual-line,[155] depressed-cladding,[156] and optical-lattice-like waveguides[157] is almost polarization independent. In addition, BiB_3O_6,[160] Nd:KGW,[164] and $KLu(WO_4)$[166] crystals belong to the monoclinic system, another member of the lower-symmetry family. In these crystals, femtosecond laser-written waveguides mainly focus on the depressed-cladding configuration, which allows symmetric guidance for both TM and TE polarizations due to the poor lattice symmetry. These features imply the unique modification of laser pulses on the crystals with different symmetries.

2.4 Mode Modulation

In recent years, numerous newly developed waveguide geometries that allow mode modulation and guiding polarization engineering have been demonstrated, benefiting from the rapid and direct prototyping of femtosecond laser writing.

For type I modification, the multiscan technique offers a flexible manner to tailor the mode profiles by controlling the number and separation of laser-induced tracks[91] [Fig. 7(a)]. In addition, by arranging the laser-modified tracks into an annular ring, the ring-shaped mode profiles in BGO crystal have also been obtained,[136] as shown in Fig. 7(b). In particular, such a design allows for polarization-independent guiding, which is different from single- and multiline type I waveguides that only support one special polarized guiding. In addition, the rings can be inscribed in the desired diameter to meet the practical applications. Theoretically, one could realize mode modulation with arbitrary geometries by proper design and arrangement of the laser-induced tracks.

As for type II modification, one can fabricate a series of dotted lines along the horizontal direction via multiscan, modulating the modal profiles along the TE polarization owing to the changed stress field distribution,[167] as shown in Fig. 7(c). At recent reports in SiC crystal, the mode modulation of waveguides has also been achieved by controlling the morphology of laser-induced tracks.[143] In addition, femtosecond laser-written waveguide arrays based on type II modification can implement mode modulation via the effect of evanescent coupling. For example, the one-dimensional planar waveguide laser arrays in Nd:YAG crystals support flexible discrete diffraction by adjusting the coupling condition.[170] Zhang et al.[37] reported the 2D waveguide arrays in $LiNbO_3$ crystal, where the output mode profiles can be modulated as the pump beam goes into the array at different positions.

Beyond the above reports, some designs based on the depressed-cladding structures also enable mode modulation. Sun et al. proposed an "ear-like" waveguide structure with extra tracks at the sides of cladding, which is an evolved scheme of double-line and depressed-cladding waveguides that was first reported by Okhrimchuk et al.[171] Such a design is intended to further enhance the optical confinement of the light field. Therefore, more symmetric mode profiles and lower propagation losses are preferred compared with the normal cladding waveguides,[168] as shown in Fig. 7(d). Another interesting sample is the double-cladding waveguide [Fig. 7(e)], which is composed of two concentric tubular shapes with different diameters.[172] One of the advantages is that the outer cladding could enhance the coupling efficiency of the pump beam and inner cladding permits an output beam with low-order modes, i.e., generating an integrated single-mode laser system.[169] Moreover, using a third-cladding structure, Wu et al.[132] demonstrated annular ring waveguide lasers, promising for complex integrated pump sources to alleviate thermal lensing.

3 Designs for Laser-Written 3D Crystalline Photonic Devices

New emerging photonic devices with 3D configurations have attracted considerable attention. Femtosecond laser writing, as the most efficient technique for true 3D microfabrication, allows an arbitrary geometry in almost any transparent substrate. Although various laser-written 3D structures have been successfully fabricated in glass,[34,173–177] the complexity of lattice and anisotropies make it much difficult to manipulate in crystals. Special designs are, therefore, required by varying the writing parameters and track geometries. In this section, we will overview the recent reports on waveguide-based 3D photonic structures, such as Y-branches, beam steering elements, ring-shaped transformers, polarizers, tapered structures, and directional couplers.

3.1 Y-Branches

As the basic 3D components, a Y branch-based splitter allows for dividing the single-input beam into several output beams in different dimensions. For example, the 3D waveguide beam splitters (1×4) based on type-I modification have been realized in $LiNbO_3$[88] and BGO crystals,[89] whereas the polarization-dependent properties are very different for the two crystalline waveguides. The $LiNbO_3$ only supports light propagation along particular orientations, whereas wave guidance in BGO is isotropic for any transverse polarization. As for type-II modification, Y-branches work well in a relatively simple way for 2D structures, as reported in diamond[178] and YAG crystals.[97] However, in the 3D case, disadvantages are emerging due to the unbalanced guiding properties and additional architecture required to connect separate channels. Moreover, the geometry of depressed cladding supports wave-guiding along any polarization, and for 3D fabrication it also requires a complicated design. The buried Y-junctions based on circular and rectangular depressed-cladding geometries have been proposed in YAG[179,180] and Ti:sapphire crystals,[181] as shown in Figs. 8(a)–8(e), which produce smooth transitions and preserve modal profiles. Furthermore, Ajates et al. reported the novel 3D beam splitting based on depressed-cladding architecture in $LiNbO_3$ crystals [Fig. 8(f)], realizing the desired 3D guiding path.[182] Although the TM-polarized modes have higher losses than that of TE, the 3D structures work well in the near-infrared band. It is possible to implement any arbitrary 3D photonic circuit in crystalline materials based on circular cladding waveguides.

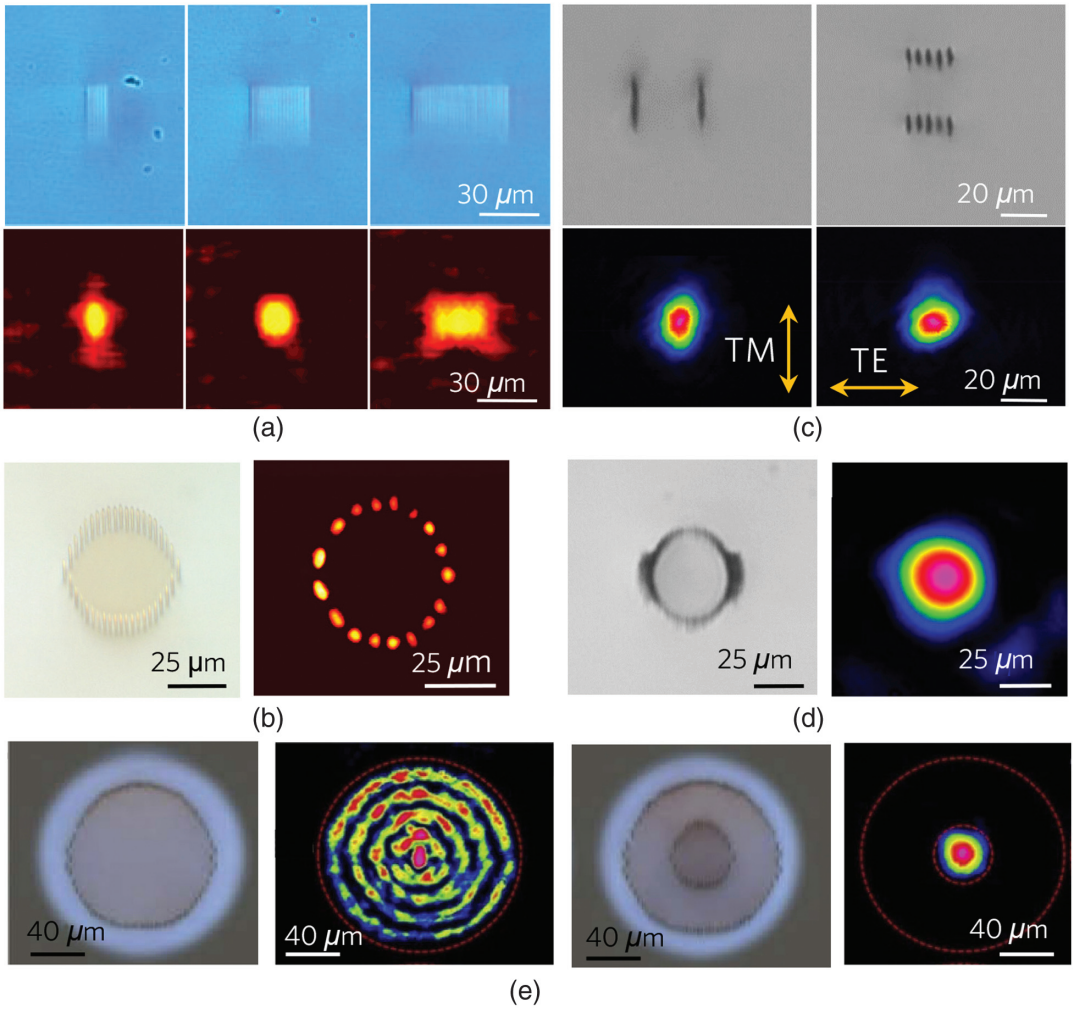

Fig. 7 (a) Microscope images and modal profiles of tailored multiline waveguides in a $LiNbO_3$ crystal, reproduced with permission from Ref. 91, © 2018 Elsevier. (b) Ring-shaped waveguide based on type-I modification in a BGO crystal, reprinted with permission from Ref. 136, © 2017 OSA. (c) Polarization engineering for dual-line waveguides in a $LiNbO_3$ crystal, reproduced with permission from Ref. 167, © 2020 Elsevier. (d) The "ear-like" waveguide in Nd:YAG crystal, reprinted with permission from Ref. 168, © 2021 OSA. (e) Double-cladding waveguide in Nd:YVO_4 crystal, reprinted with permission from Ref. 169, © 2019 OSA.

3.2 Photonic-Lattice-Like Structures for 3D Microfabrication

Additional branched boundaries are essential for beam splitters in Sec. 3.1; as a result, the fabrication processing is usually time-consuming. To this end, the family for 3D microfabrication is designed, known as an "optical-lattice-like" photonic structure, which contains a number of periodic tracks with geometry defects. A typical structure has a track layer of hexagonal layout, where the light field is confined at enclosed track-free regions. Particularly, better guiding confinement is followed at multilayers rather than single layer. Tailored beam steering in the 3D manner, such as beam splitting or ring-shaped transformation,[100] can be realized by directly introducing additional defect tracks at certain positions. These defect lines served as beam blocks or confiners that smoothly reshape the guiding profiles during the propagation; therefore, no additional losses are introduced.[102] Based on this strategy, 3D beam steering of ring-shaped transformation has been successfully inscribed in YAG crystals,[100] as shown in Figs. 9(a) and 9(b). In addition, highly compact 3D beam splitters ($1 \times N$) have been implemented in many platforms, such as $LiNbO_3$,[145] $KTiOPO_4$,[157] Nd:YAG, and Ti-sapphire crystals[153] [Figs. 9(c)–9(e)]. By carefully considering the crystalline properties, more advanced applications, such as nonlinear frequency conversion[183] and miniature laser sources have been demonstrated.[101] Such 3D designs could efficiently improve the integration of complex photonic circuits. Considering the huge differences in the characteristics of crystals, however, each type requires a different 3D inscription and feasible optimization scheme.

3.3 3D Polarizers

In photonic integrated circuits (PICs), the undesirable effect of polarization dependence limits the practical applications of polarization-division multiplexed systems. Hence, polarization

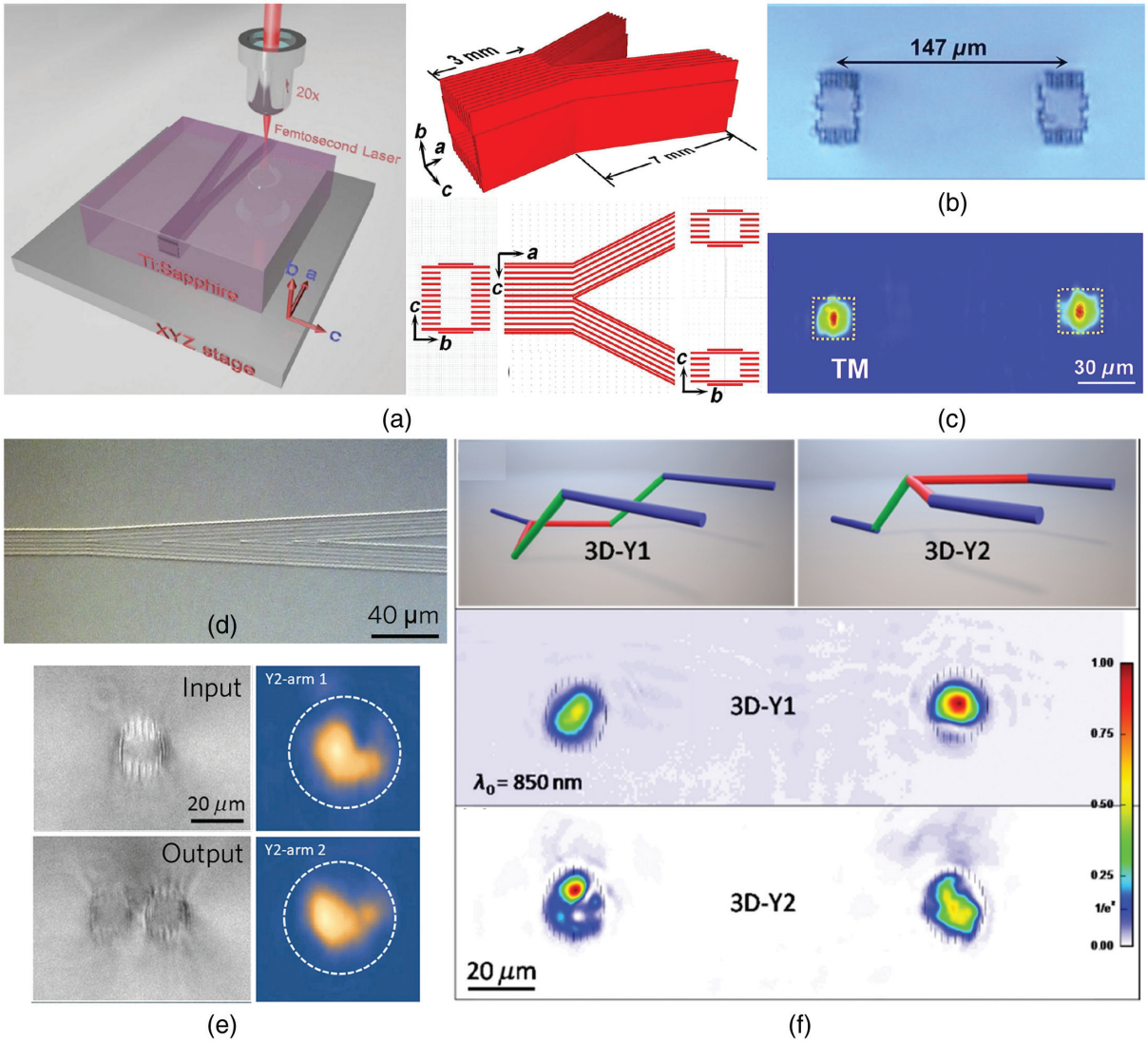

Fig. 8 (a) Fabrication and 3D schematic diagram of Y-splitters based on rectangular cladding geometry in Ti:sapphire crystal, (b) microscope image of 1-deg branching angle, and (c) intensity distributions at 1064 nm. Images (a)–(c) are reproduced with permission from Ref. 181, © 2018 Elsevier. Microscope images of Y-branch with circular cladding structure (d) in top view and (e) in cross section, as well as modal profiles of two arms. Images (d) and (e) are reproduced with permission from Ref. 179, © 2017 Elsevier. (f) 3D beam-splitting structures in a $LiNbO_3$ crystal, reprinted with permission from Ref. 182, © 2018 Optica.

diversity devices including polarizers, polarization beam splitters (PBSs), and polarization rotators attract researchers' interest. Femtosecond laser writing provides an on-demand fabrication method for polarization photonic devices. Recently, a new structure of polarizer has been employed to engineer the guiding polarization in $LiNbO_3$ crystals,[184] as depicted in Figs. 10(a) and 10(b), which is composed of three parts: a rectangular-shaped channel, a 1×2 beam splitter acting as the connection element, and two output channels. In such a structure, the output will be well-separated into TE and TM polarized light as the polarized light or hybrid light of TE plus TM modes enters the waveguide [Fig. 10(c)]. The polarization extinction ratio and insertion loss can be comparable with that of fused-silica-based PBS. In addition, a 3D polarizer in a cross-shaped geometry has been produced in $LiNbO_3$ crystal,[167] consisting of a square cladding waveguide and four vertically oriented double lines [Figs. 10(d) and 10(e)]. This 3D configuration enables specific polarized-light output at different waveguide arrays, i.e., the TM or TE-polarized light can be controllably coupled into vertical or horizontal waveguide arrays, respectively.

3.4 Other Schemes

Tapered waveguide structures, like the tapered optical fibers, have different circular radii of input and output arms. In 2020, Romero et al.[185] proposed a 3D tapered waveguide by smoothly decreasing the separation between the tracks that consisted of the depressed-cladding waveguide, as shown in Fig. 11(a). This approach enables the desired reduction of the input/output

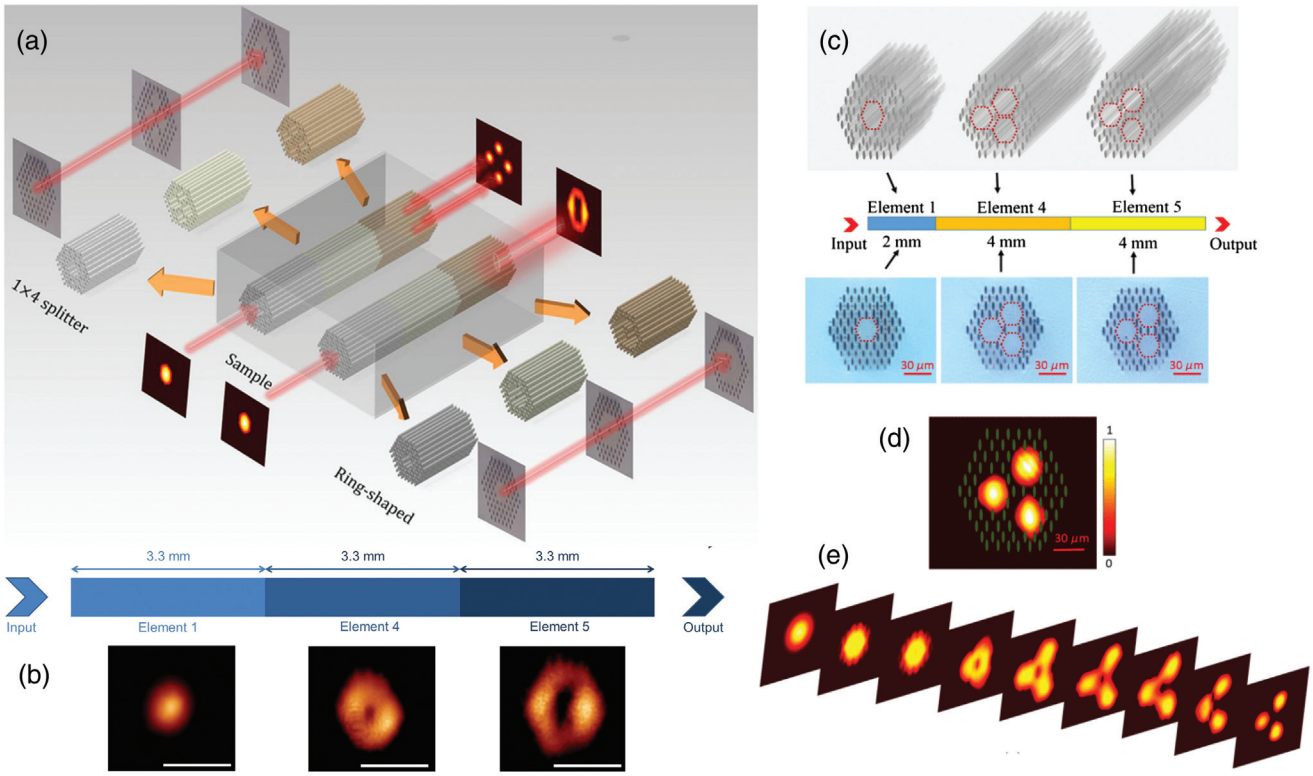

Fig. 9 (a) Schematic illustration of 1×4 beam splitting and ring-shaped transformation based on photonic-lattice-like structures. Image (a) is reproduced from Ref. 102. (b) Measured evolution of ring-shaped transformation in a Nd:YAG crystal. The scale bar is 50 μm. (c) Prototype design and microscope images of 1×3 beam splitters in a $LiNbO_3$ crystal, (d) measured and (e) simulated modal profile. Images (c)–(e) are reprinted with permission from Ref. 145, © 2016 IEEE.

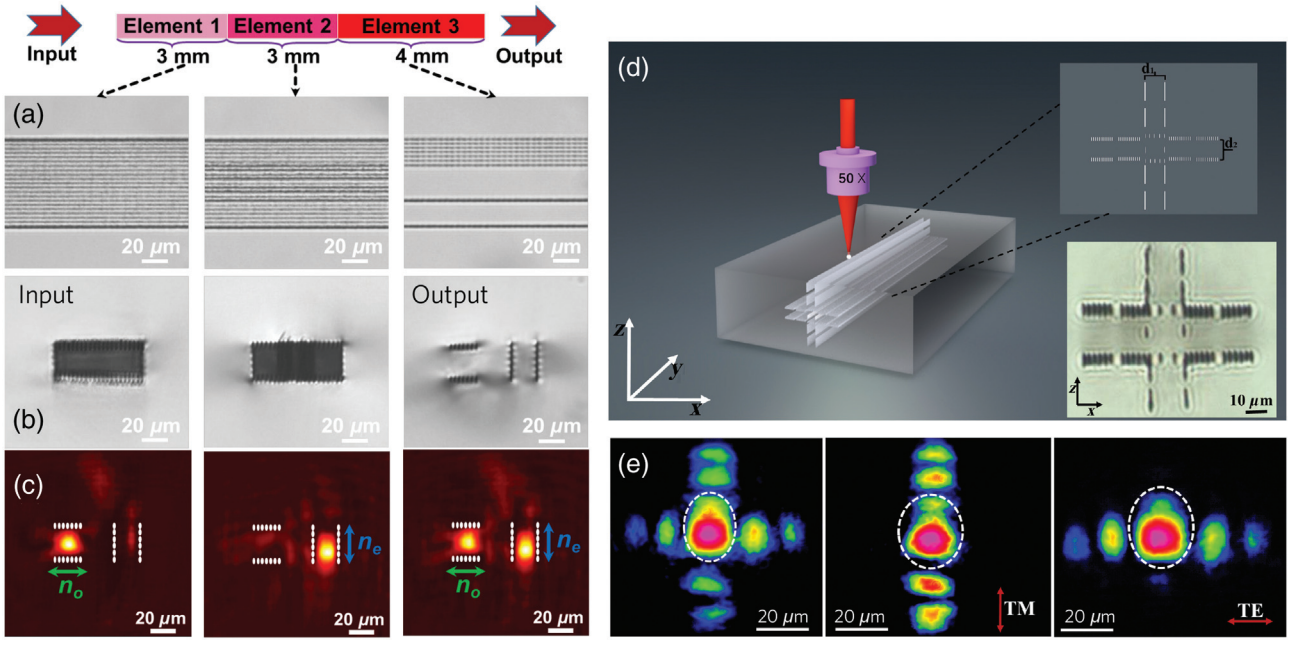

Fig. 10 (a) Microscope images in top view, (b) end-face of polarization beam splitters, and (c) modal profiles along n_0, n_e, and circular polarizations, respectively. Images (a)–(c) are reprinted with permission from Ref. 184, © 2020 IEEE. (d) Schematic plot and microscope images of 3D polarizer. (c) Modal profiles at different polarizations. Images (d) and (e) are reprinted with permission from Ref. 167, © 2020 IEEE.

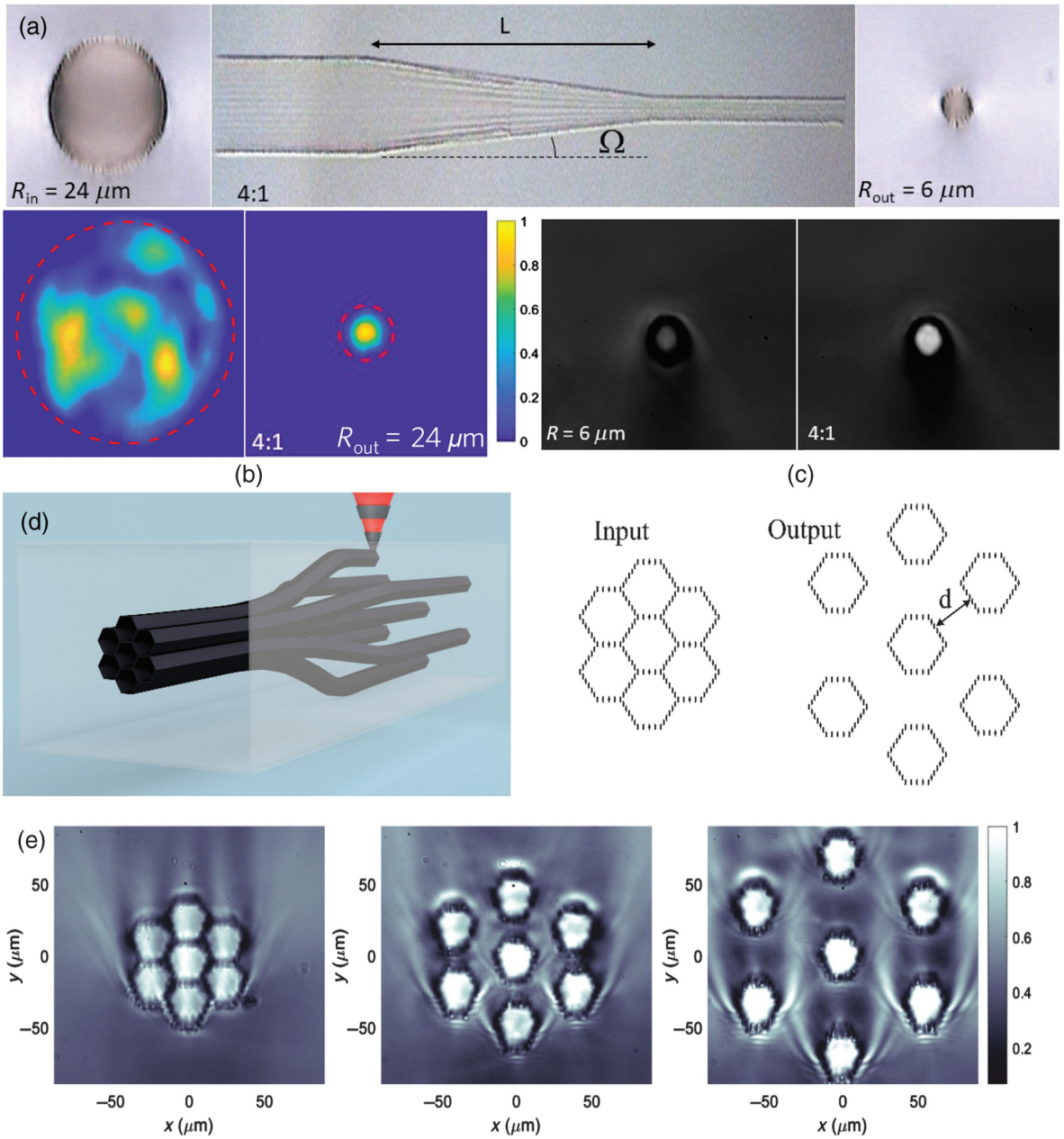

Fig. 11 (a) Microscopic pictures of a tapered cladding waveguide in a Nd:YAG crystal and (b) modal profiles at the input radii of 24 μm and output of 6 μm, respectively. (c) Modal profiles of a straight and tapered waveguide at the same output radii from an incident LED light, reproduced with permission from Ref. 185, CC-BY. (d) Prototype of depressed-cladding 3D waveguide arrays. (e) Optical micrographs at the output face for different separations between the central and adjacent waveguides. Images (d) and (e) are reprinted with permission from Ref. 186, © 2017 IEEE.

radius, allowing highly multimodal coupling into single-mode waveguides, as depicted in Fig. 11(b). It is particularly interesting for waveguide laser systems, which reaches a higher coupling efficiency of the pump beam and enhanced intensity of the output power compared to a straight waveguide with the same radius. In addition, such a 3D design offers an efficient manner for modal formatting or light concentration [Fig. 11(c)]. Another promising scheme is the 3D waveguide array,[37] which has a potential application in 3D photonic devices, such as photonic lanterns. Figure 11(d) illustrates the prototype of 3D waveguide arrays in Nd:YAG crystals,[186] which are composed of seven adjacent hexagonal cladding structures at the input face and have each waveguide separated radially from the center at a certain distance at the output face, as shown in Fig. 11(e). This design shows a good wave guiding for both the visible and near-infrared bands. The directional coupler is the basic building block for integrated classical and quantum photonic circuits.[45] Figure 12(a) presents the 3D design of a 3 × 3

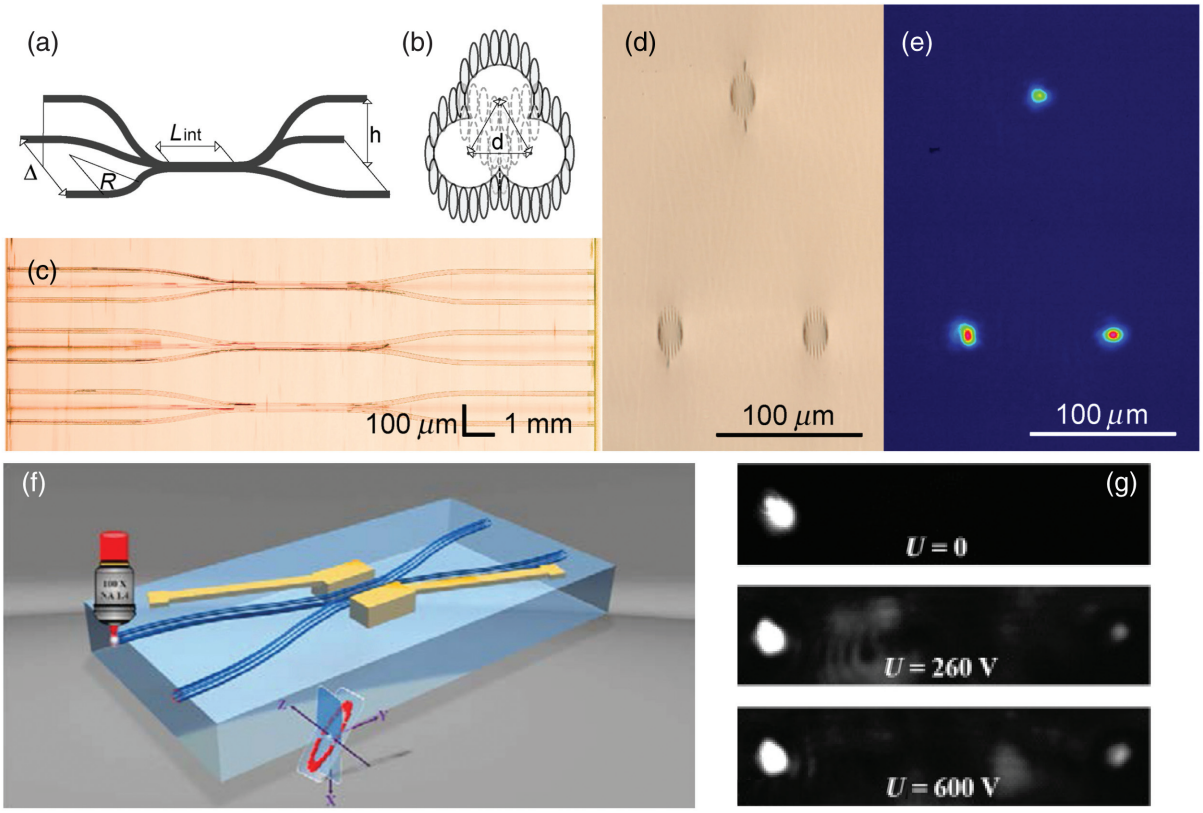

Fig. 12 (a), (b) Geometry and cross-section design in the interaction region of the 3 × 3 directional coupler in a Tm^{3+}:YAG crystal. (c), (d) Top and output view microscope images and (e) output intensity distribution. Images (a)–(e) are reproduced with permission from Ref. 187, CC-BY. (f) Schematic plot of 2 × 2 directional coupler integrated with 3D microelectrodes in a $LiNbO_3$ crystal. (g) Output intensity profiles with different voltages. Images (f) and (g) are reprinted with permission from Ref. 118, © 2019 CLP.

directional coupler based on a depressed-cladding waveguide in a Tm^{3+}:YAG crystal[187] in which several cladding tracks are removed to form the coupling region [Fig. 12(b)]. The top and cross-section view microscope images are shown in Figs. 12(c) and 12(d). Single-mode guidance with an output splitting ratio of 19:40:41 at 810 nm was demonstrated in this work [Fig. 12(e)], indicating the potential applications in quantum storage devices. By integrating embedded 3D electrodes on both sides of the coupling region of the buried directional coupler in a $LiNbO_3$ crystal,[118] as shown in Fig. 12(f), the efficiency of electro-optic modulation was finely improved [Fig. 12(g)].

4 Selected Applications

In recent years, direct femtosecond laser writing of dielectric crystals enables various waveguiding structures, offering an ideal platform for a broad range of photonic applications by considering the bulk properties of the materials used. In this section, selected advances in recent applications of laser-written crystalline waveguides are overviewed.

4.1 Waveguide Lasers

Benefitting from the high optical confinement, femtosecond laser-written waveguides provide efficient miniaturized laser sources that cover the spectral range from visible to MIR (530 nm to 4 μm) with many advantages, such as reduced lasing thresholds, enhanced slope efficiencies, compact size, nondiffraction beams, and multifunctional integration.[7] Up to now, some notable improvements have been achieved, depending on the active ions and the mechanisms for lasing. Table 3 summarizes the reported results for waveguide lasers emitting at different wavelengths based on various cavity designs fabricated in femtosecond laser writing.

Laser emission at visible wavelengths mainly relies on Pr^{3+}-doped gain media, such as $Pr:SrAl_{12}O_{19}$, $Pr,Mg:SrAl_{12}O_{19}$, and $Pr:LiYF_4$ crystals. For instance, using well-established dual-line structure, a green waveguide laser operating at 525.3 nm was first demonstrated in $Pr,Mg:SrAl_{12}O_{19}$ crystals.[190] Since then, based on the rhombic cladding geometry, orange and deep red laser oscillations at 604 and 720 nm were produced in $Pr:LiYF_4$ crystal.[191] Moreover, laser-written active dual-line waveguides in Ti:sapphire have offered tunable laser operating from 700 to 870 nm.[192] In addition, with the same dual-line configuration in Ti:sapphire, Grivas et al.[152] reported a femtosecond continuous-wave mode-locked (CWML) laser emitting at 790 nm. The generated waveguide laser was operated at pulses of 41.4 fs with a fundamental repetition rate up to 21.25 GHz.

Near-infrared spectral range is the most common laser emission band, which is gained by writing an active waveguide into well-known Nd^{3+}- and Yb^{3+}-doped crystals. Beyond a normal straight laser cavity, it is also possible to achieve efficient optical

Table 3 Summary of reported results for waveguide lasers emitting at different wavelengths based on various laser-cavity designs.

					Laser performance			
Wavelength band	Gain media	Working wavelength (nm)	Cavity configuration	Operation regime	Lasing threshold (mW)	Max. output power (mW)	Slope efficiency	Ref.
Visible	Nd:YCOB	531	Cladding	CW	5	0.1	—	161
	Nd:YAB	532	Dual line	CW	—	0.032	—	188
	Pr:$SrAl_{12}O_{19}$	634.5	Dual line	CW	190	28.1	8%	189
	Pr, Mg:$SrAl_{12}O_{19}$	525.3	Dual line	CW	1088	36		190
		644			516	1065	37%	
		724.9			885	504	25%	
	Pr:$LiYF_4$	604	Rhombic cladding	CW	360	25	5.6%	191
		720			243	12	2.0%	
	Ti : sapphire	700 to 870	Dual line	CW	84	143	23.5%	192
		798.5	Dual line	CWML (21.25 GHz)	1160.1	87.48	—	152
Near-infrared	Yb, Na:CaF_2	1013.9 and 1027.9	Cladding	CW and *Q*-switched	152.2	26.6	10%	193
	Yb : YAG	1030	S-curved dual line	CW	141	1 W	79%	194
			Y-branch dual line	CW	271	2.29 W	52%	97
			Dual line	*Q*-switched	102	5.6 W	74%	195
			Dual line	QML (2 GHz)	1800	322	11.3%	196
			Double cladding	CW	401.7	45.8	38%	172
	Yb : KLuW	1040	Surface cladding	*Q*-switched	491	680	61%	197
	Nd : YAG	1064	Annular ring shaped	CW	191	84	20%	132
			Ear-like cladding	CW and *Q*-switched	10	327	34.4%	168
			Cladding	*Q*-switched	287	102.3	11.9%	198
				QML (8.8 GHz)	74	127	26%	199
		1061.58 and 1064.18	Cladding	CWML (9.8 GHz)	—	530	—	200
		1064	Y-branch cladding	CW	231	172	22.4%	180
			1 × 2 splitters	CW	90	333	34%	101
			1 × 4 splitters		90	217	22%	
			Ring shaped	CW and *Q*-switched	148	224	22%	100
	Nd:YVO_4	1064	Cladding	CW	10.3 W	3.4 W	36%	139
				Q-switched	57.4	275	37%	201
				QML (6.5 GHz)	65	424	56%	202
				CWML (6.5 GHz)	19.3	259	30.6%	203
			Double cladding	*Q*-switched	59	397	46%	169
			Optical-lattice like	*Q*-switched	—	85	20%	140
	Nd : YAP	1064 and 1079	Cladding	CW	243	199.8	33.4%	158
			S-curved cladding	QML (7.9 GHz)	196	77	14.1	159
			S-curved optical-lattice like		228	57	10.69	
		1072 and 1079	Optical-lattice like	CW	384.5	101.3	30.9	75
	Nd:$GdVO_4$	1063.6	Dual line	CW	52	256	70%	141
		1064.5	Cladding	CW and *Q*-switched	178	570	68%	142
	Nd : GGG	1061	Dual line	CW	29	11	25%	134
		1063	Cladding	CW	270	209	44.4%	135
	Nd:$LuVO_4$	1066.4	Dual line	CW	98	30	14%	204
	Nd : KGW	1065	Dual line	CW	141	33	52.3%	163
		1067	Cladding	CW	120	198.5	39.4%	164

Wavelength band	Gain media	Working wavelength (nm)	Cavity configuration	Operation regime	Laser performance			Ref.
					Lasing threshold (mW)	Max. output power (mW)	Slope efficiency	
MIR	$Tm:KLu(WO_4)_2$	1847.4	Surface cladding	CW	52	171.1	37.8%	205
		1846.8		*Q*-switched	500	150	34.6%	
		1849.6	Cladding	CW	45	247	48.7%	206
		1844.8		*Q*-switched	—	24.9	9.3%	
		1847	Optical-lattice like	CW	21	46	9.9%	207
		1841 to 1848	Y-branch cladding	CW	280	460	40.6%	208
	Tm : YAG	1943.5	Cladding	QML (7.8 GHz)	665	6.5	2%	209
	$Ho:KGd(WO_4)_2$	2055	Cladding	CW	180	212	67.3%	210
	$Tm:MgWO_4$	2080	Surface cladding	CW	120	132	38.9%	211
	Ho : YAG	2091	Cladding	QML (5.9 GHz)	—	170	6.8%	212
		2096		CW	100	1775	16%	213
	Cr : ZnS	2333	Cladding	CW	450	101	20%	214
	Cr : ZnSe	2522	Cladding	CW	—	5200	41%	215
	Fe : ZnSe	4070	Cladding	CW	—	995	58%	

feedback for lasing oscillation in curved and branched cavity geometry owing to an enhanced optical gain of a waveguide laser. For example, in femtosecond laser-written 3D structures, compact waveguide lasers at 1 μm have been proposed in different functionalities, such as S-curved,[159,194] Y-branches,[97,180,208,216] 1×2 and 1×4 beam splitting,[101] ring-shaped beam transformation,[100,132] and optical-lattice-like lasing[75] [Figs. 13(a)–13(e)]. Laser performance in these reports is comparable to that of straight waveguides, suggesting a superior flexibility for prototyping laser sources using femtosecond laser writing. By further integrating a suitable absorber, passively *Q*-switched lasing has been realized. For example, using a high gain Yb:YAG channel waveguide, an efficient *Q*-switched laser has shown a slope efficiency of 74% with an average power up to 5.6 W in a single-pass optical pumping without any reflective mirrors.[195] Most recently, mode-locked waveguide lasers operating at multi-gigahertz (GHz) regimes have attracted increasing interest. For instance, 6.5 GHz *Q*-switched mode-locked (QML) lasers have been demonstrated in a femtosecond laser-written $Nd:YVO_4$ cladding waveguide using 2D materials as the saturable absorber.[202] Another recent sample is Nd:YAP crystal : 31.6-GHz QML lasers have been demonstrated in an S-curved waveguide,[159] as shown in Fig. 13(f). In particular, both single- and dual-wavelength (1064 and 1079 nm) lasing can be achieved by tuning the pump polarization [Figs. 13(g) and 13(h)].

Recently, MIR (~2 μm) waveguide lasers, typically obtained from Tm^{3+}- and Ho^{3+}-doped materials, have attracted much attention from researchers. For a gain medium of $Tm:KLu(WO_4)_2$, efficient waveguide lasers at ~1.8 μm operating both in the CW and *Q*-switched regimes have been reported by Kifle et al. in various laser-written waveguide structures, such as Y-branch splitters,[208] surface cladding,[205] buried circular cladding,[166,206] and photonic-lattice-like cladding prototypes.[207] In addition, their group has demonstrated a low-loss (<0.1 dB/cm) waveguide laser in a $Tm^{3+}:MgWO_4$ crystal at ~2.02 μm with a slope efficiency of 64.4%.[211] Also, in the multi-GHz operation regime, 5.9- and 7.8-GHz QML waveguide lasers at ~2 μm have been successfully achieved in $Ho^{3+}:YAG$[212] and Tm : YAG,[209] respectively. Cr:ZnS is another host medium for MIR laser generation. Based on the cladding channel waveguide, an efficient 2333-nm waveguide laser with an output power of 101 mW has been reported by Macdonald et al.[214] Moreover, waveguides written in Fe:ZnSe crystal have shown a slope efficiency of 58%, offering a working wavelength up to 4070 nm.[215]

4.2 Frequency Converters

Frequency conversion displayed in femtosecond laser-written waveguides coming from second and higher-order nonlinearities offers an efficient manner to access special wavelengths. Similar to waveguide lasers, frequency converters in waveguide structures provide enhanced conversion efficiencies compared to bulk material, as a result of strong optical confinement and good overlap between the fundamental and nonlinear polarization waves over the whole interaction length. Femtosecond laser-written waveguides allow for nonlinear optical conversion, mainly SHG, at a wavelength range between ~400 and 790 nm.

One of the most well-studied nonlinear crystals is $LiNbO_3$, since the work of Burghoff et al.[217] in 2007, which enabled efficient frequency doubling of 1064 nm with a conversion efficiency of 49% in laser-written dual-line waveguides. In 2021, using the regime of birefringent phase matching (BPM), waveguide geometries of multiline, vertical dual line, and depressed cladding have also been reported in $LiNbO_3$ crystals for SHG of 1064 nm,[218] whereas BPM is difficult to realize in some crystals with weak birefringence. In recent years, LiQPM grating structures have attracted a particular interest in frequency doubling, beginning from the first proof in 2013 reported by Thomas

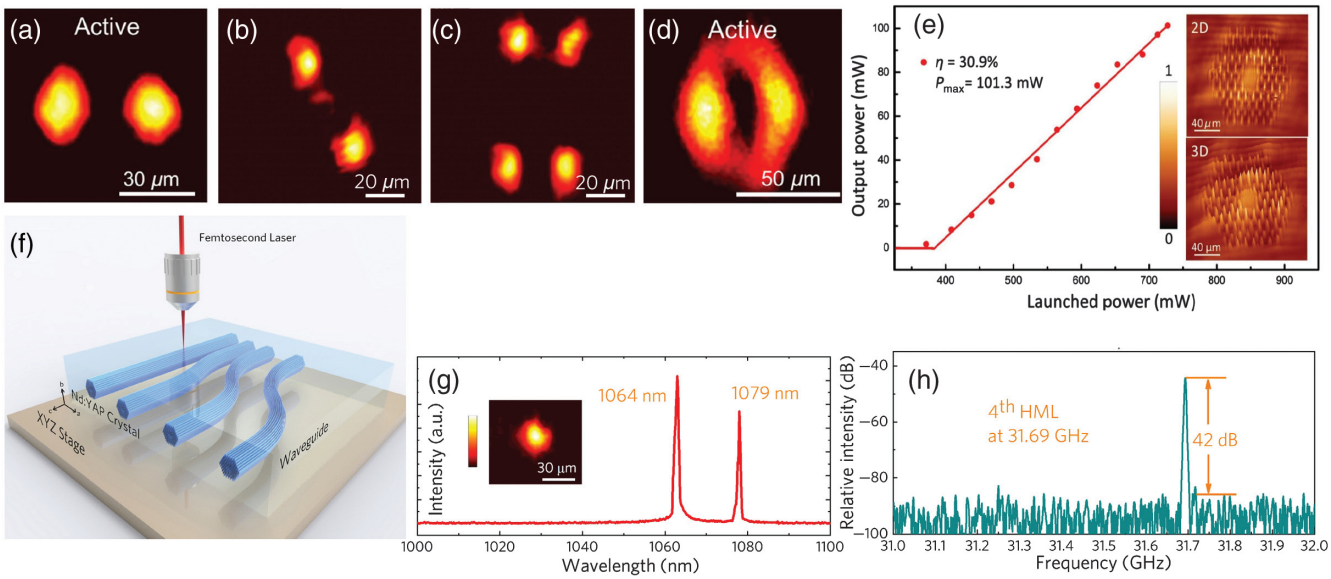

Fig. 13 Complex waveguide laser modal profiles at 1 μm: (a), (b) Y-branches, (c) 1 × 4-branch, (d) ring-shaped transformation, and (e) optical-lattice-like. Images (a) and (d) are reproduced with permission from Ref. 100. Images (b) and (c) are reprinted with permission from Ref. 101, © 2016 IEEE. Image (e) is reprinted with permission from Ref. 75, © 2016 OSA. (f) Schematic illustration of the fabrication process of an S-curved waveguide, (g) laser spectra of dual-wavelengths at 1064 and 1079 nm, and (h) RF spectrum of modelocking at 31.69 GHz. Images (f)–(h) are reprinted with permission from Ref. 159, © 2020 IEEE.

et al.[119] though with a poor conversion efficiency. Later in 2015, an increased conversion efficiency of 5.72% was reported by Kroesen et al., which introduced QPM grating structure inside a depressed-cladding waveguide.[127] In 2020, a waveguide-integrated 3D QPM grating scheme was proposed, as shown in Fig. 14(a), thus multiwavelength SHGs of 1065.3, 1064, 1061.6, and 1060.5 nm radiation have been demonstrated[43] [Fig. 14(b)]. Using this technique, Wei et al.[121] produced 3D NPC in $LiNbO_3$ crystals, as well as realizing an SHG of 829 nm with an enhanced second-harmonic power compared with the on-engineered area. Figure 14(c) illustrates the setup of the SHG process using LiQPM structures in quartz crystal, and a deep-ultraviolet generation of 177.3 nm has been achieved with a high efficiency of 1.07%$_o$[124] [Fig. 14(d)]. In addition, based on a type I single-line waveguide, the green-up conversion at 550 and 528 nm and NIR emission at 1550 nm have been reported in $Er:MgO:LiNbO_3$ crystals.[144] Moreover, spontaneous parametric down-conversion from 780 to 1560 nm has also been demonstrated in laser-written multiline waveguides of PPLN crystal, giving access to photon entanglement in quantum technologies.[49]

Frequency doubling down to ultraviolet bands has also attracted much attention. BiB_3O_6 cladding waveguide is a good sample, and a violet SHG at 400 nm has been realized.[219] $LiTaO_3$ crystal is another promising material owing to its shorter cut-off wavelength (0.28 μm) and high optical damage threshold. In 2019, a second harmonic power up to 8.5 W was realized in laser-written circular-cladding waveguides under a CW pump at 1050 nm in a periodically poled $MgO:LiTaO_3$ (PPMgSLT) crystal.[220] Figure 14(e) depicts the schematic plot of femtosecond laser direct writing cladding waveguides in fan-out PPMgSLT crystals, corresponding to different poling periods. Temperature-tuned SHG for different QPM periods has been demonstrated in Fig. 14(f) with a comparable normalized conversion efficiency of 3.55% $W^{-1}cm^{-2}$.[148] Later in 2020, a tunable violet SHG over the range of 396 to 401 nm was demonstrated by varying the QPM condition in fan-out PPMgSLT crystals,[221] evincing efficient frequency converters based on femtosecond laser-written waveguides.

$KTiOPO_4$ (KTP) is another excellent nonlinear platform for frequency conversion. In 2007, the laser-written multiline waveguide based on type I modification permitted SHG down to 400 nm in periodically poled $:KTiO_PO_4$ (PPKTP) crystals.[154] Lately, a further improvement of conversion efficiency (4.6% W^{-1} cm^{-2}) has been proposed in type II dual-line waveguides in Rb-doped PPKTP crystals.[222] In particular, due to the true 3D micromachining of femtosecond laser writing, optical lattice-like 1 × 4 beam splitters in KTP crystals have enabled SHG of 1064 nm by BPM.[157] In addition, the optical-lattice-like microstructures offer an efficient manner for beam mode controlling, providing a simple way to realize single-mode frequency doubling at 532 nm with a comparable conversion efficiency.[183] Table 4 summarizes the latest results for frequency converters based on femtosecond laser-written waveguides.

4.3 Quantum Memories

To date, femtosecond laser direct writing has played an important role in integrated quantum information processing,[225,226] such as integrated sources of entangled photons,[49] high-dimensional transmission of quantum twisted light states,[47] 2D quantum walk,[46] and the rotated polarization directional coupler.[45] Quantum memories (QMs) are essential components in large-scale quantum networks, especially in quantum repeaters. Rare-earth ion-doped crystals are promising candidates of integrated

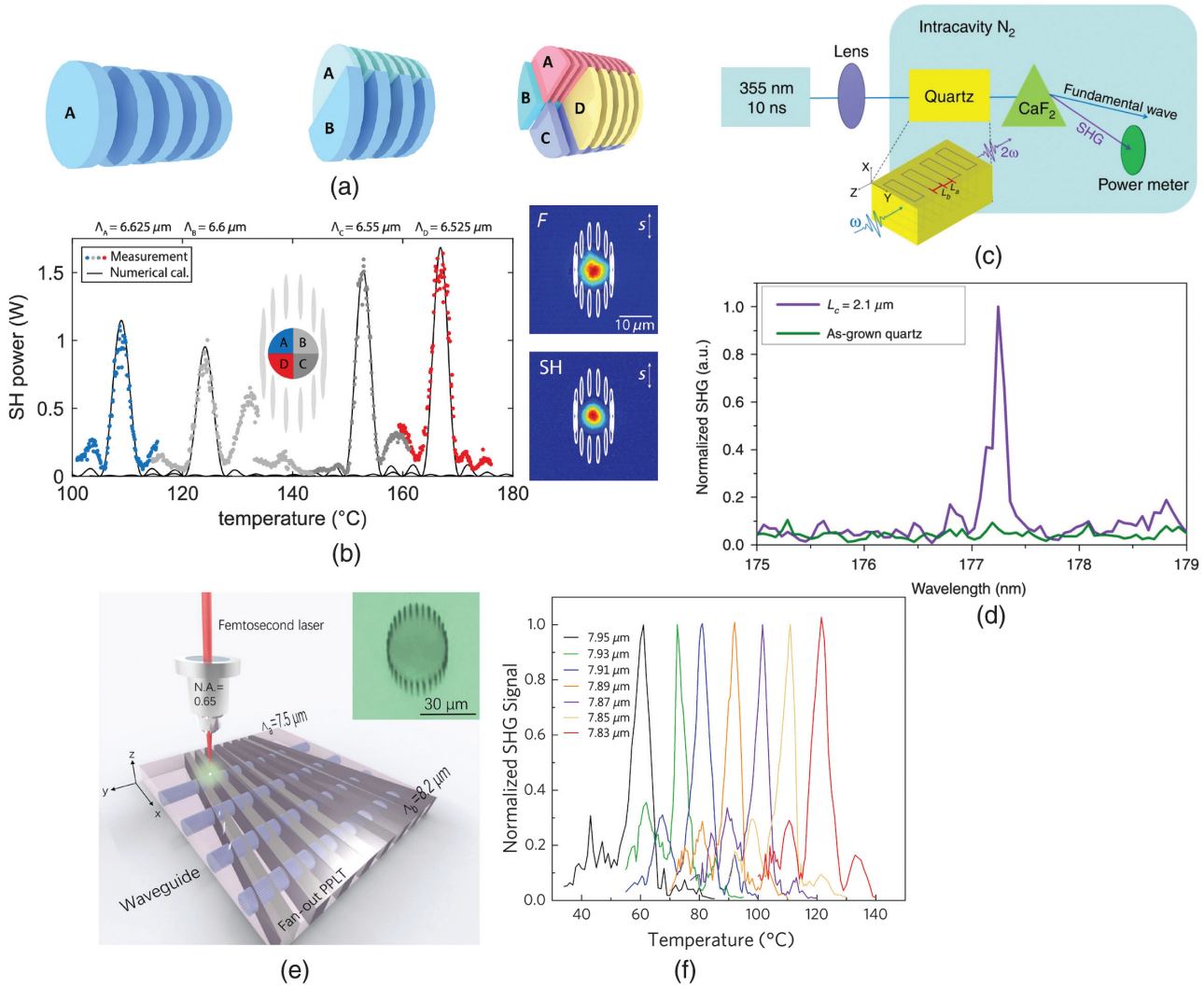

Fig. 14 (a) Waveguide-integrated 3D LiQPM scheme, one period, two periods, and four periods in a $LiNbO_3$ crystal. (b) Simultaneous SHG of four wavelengths and the fundamental and second harmonic modal profiles of a single period. Images (a) and (b) are reprinted with permission from Ref. 43, © 2020 OSA. (c) Experimental setup of the ultraviolet SHG process using LiQPM structure in a quartz crystal and (d) the SHG response signal of 177.3 nm. Images (c) and (d) are reproduced with permission from Ref. 124, CC-BY. (e) Schematic diagram of femtosecond laser-written cladding waveguide in a fan-out PPSLT crystal and (f) temperature tuning curves of seven waveguides with different poling periods. Images (e) and (f) are reprinted with permission from Ref. 148, © 2019 OSA.

QMs due to their large bandwidth, high multimode capacity, and high storage fidelity.[227] Two approaches have been employed to manufacture integrated QMs in rare-earth ion-doped crystals, such as Ti-indiffusion in $LiNbO_3$[15] and focused-ion-beam milling.[228] Nevertheless, the storage time and efficiencies in these two systems are significantly reduced. In recent years, femtosecond laser direct writing has allowed channel waveguides with improved capabilities, where the active ions are directly coupled to the light, rather than via evanescent coupling.[52,225,229] As a result, spin-wave storage with an extended lifetime, which enables long-term storage and on-demand readout, has been achieved in waveguide-integrated QMs.[50,51,53,230] A great amount of effort has been devoted to this topic, mainly focused on the geometry of type I, type II, and ridge waveguides.

The first proof of QMs based on laser-written dual-line waveguides was reported in $Pr^{3+}:Y_2SiO_5$ crystals, where the interaction with the active ions is increased by a factor of 6 compared to bulk, and demonstrated a spin-wave optical memory,[229] as shown in Figs. 15(a)–15(d). Later in 2020, using the type II waveguides in $Eu^{3+}:Y_2SiO_5$ crystals, on-demand light storage was demonstrated via the spin-wave atomic frequency comb (AFC) and the storage fidelity was quantitatively characterized for the first time.[50] Compared to type II waveguides, the fabrication of type I waveguides in crystalline substrates is still a very challenging task, as it requires a very narrow writing window. In 2018, Seri et al.[52] produced high-quality type I waveguides in $Pr^{3+}:Y_2SiO_5$ crystals, demonstrating efficient storage times 100 times longer than previous demonstrations [Figs. 15(e)–15(g)]. In the next year, their group reported more than 130

Table 4 Summary of latest results for frequency converters in femtosecond laser-written waveguides.

Crystal	Waveguide configuration	Laser regime	λ_ω (nm)	$\lambda_{2\omega}$ (nm)	SHG configuration	P_{out} ($W^{-1}\,cm^{-2}$)	Norm. efficiency ($W^{-1}\,cm^{-2}$)	Ref.
BBO	Cladding	CW	800	400	BPM	1.05 mW	0.98%	219
PPKTP	Type I (multiscan)	CW	800	400	QPM	51 μW	0.02%	154
PPSLT	Cladding	CW	800	396 to 401 (tunable)	QPM	0.37 mW	0.39%	221
PPKTP	Dual line	CW	943.18	471.59	QPM	76 mW	4.6%	222
$LiNbO_3$	Cladding	Pulsed	1030	515	BPM	—	—	223
	Type I (multiline)	Pulsed	1064	532	BPM	12.45 W (peak)	0.27%	218
	Dual line	Pulsed	1064	532	BPM	4.95 W (peak)	0.14%	
	Cladding	Pulsed	1064	532	BPM	40.40 mW (peak)	0.87%	
	Cladding	Pulsed	1064	532	LiQPM	25.1 W (peak)	0.0637%	127
	Cladding	Pulsed	1065.3, 1064, 1061.6, and 1060.5	532.65, 532, 530.8, and 530.25	LiQPM	1.33 W (peak)	0.64% ($P_{2\omega}/P_\omega$)	43
PPMgSLT	Cladding	CW	1064	532	QPM	17.3 μW	0.74%	224
	Cladding	CW	1050	525	QPM	8.5 W	0.16%	220
	Cladding	CW	1064	532	QPM	14.87 mW	3.55%	148
	Cladding	Pulsed	1064	532	QPM	153 W (peak)	54.3% ($P_{2\omega}/P_\omega$)	
$KTiOPO_4$	Optical-lattice like (1 × 4 splitters)	CW	1064	532	BPM	0.65 mW	1.5%	157
	Optical-lattice like (straight)	CW	1064	532	BPM	0.67 mW	0.87%	
	Hybrid optical-lattice	CW	1064	532	BPM	0.8 mW	1.1%	121

individual storage modes in laser-written type I waveguides in $Pr^{3+}:Y_2SiO_5$ crystals, among the temporal, spectral, and spatial domains, demonstrating the capability of both time and frequency multiplexing single photon.[53] Such high multimodality will be necessary to realize an efficient quantum repeater scheme.

Considering that the channel waveguides (type I and type II) are fabricated at a depth beneath the crystal surface, ridge waveguide-based QMs are easily integrated with other on-chip devices, allowing for constructing large-scale quantum networks. In 2020, a laser-written ridge waveguide was successfully fabricated in an $Eu^{3+}:Y_2SiO_5$ crystal, in which the properties of the Eu^{3+} ions were well-preserved.[230] The spin-wave AFC storage was implemented, confirming high-interference visibility [Figs. 16(a)–16(d)]. In 2021, their group achieved a better fabrication parameter, realizing 40% end-to-end device efficiency, while the typical coupling efficiency is 10% in $LiNbO_3$ waveguide memory. Combined with on-chip electrodes, a high storage fidelity of $99.3\% \pm 0.2\%$ and on-demand storage of time-bin qubits were demonstrated,[51] far beyond that value of the classical measure-and-prepare strategy.

4.4 On-Chip Devices

Thin-film lithium-niobate-on-insulator (LNOI) has attracted significant interest in the field of PIC for its favorable low-loss limit and electro-optic coefficients.[17,18,231] With the recent revolution in fabrication techniques of on-chip photonics, great progress has been sparked in producing ultrahigh performance building blocks, such as waveguides[16,232] and microcavities,[233] for scalable and high-density LNOI PICs. In 2015, Lin et al.[234] first reported on the fabrication of high-Q $LiNbO_3$ microresonators by femtosecond laser direct writing, followed by focused ion beam milling. In 2018, their group proposed an efficient LNOI fabrication technique termed photolithography-assisted chemomechanical etching (PLACE).[235] Figures 17(a)–17(e) schematically illustrate the process of PLACE, including mainly five steps. Notably, femtosecond laser micromachining is used to pattern the Cr thin film into a waveguide- or circular disk-shaped mask with the advantages of high scanning speed and high quality. The key in this step is to carefully choose a peak intensity of the femtosecond laser, in which the Cr film can be completely removed without damaging the underneath LNOI, since the ablation threshold of LNOI is significantly higher than that of the metal Cr.[233] In addition, chemomechanical polishing (CMP) is employed to selectively etch smooth sidewalls capable of low scattering loss. Using this technique, a 10-cm-long LNOI waveguide with an ultralow loss of 0.027 dB/cm[232] [Figs. 17(f)–17(h)] and an LNOI microresonator with an ultrahigh Q factor of 4.7×10^7 by improving the surface roughness of ~0.115 nm[233] [Fig. 17(i)] have been demonstrated. In addition, by adding a layer of Ta_2O_5 film on the waveguides,

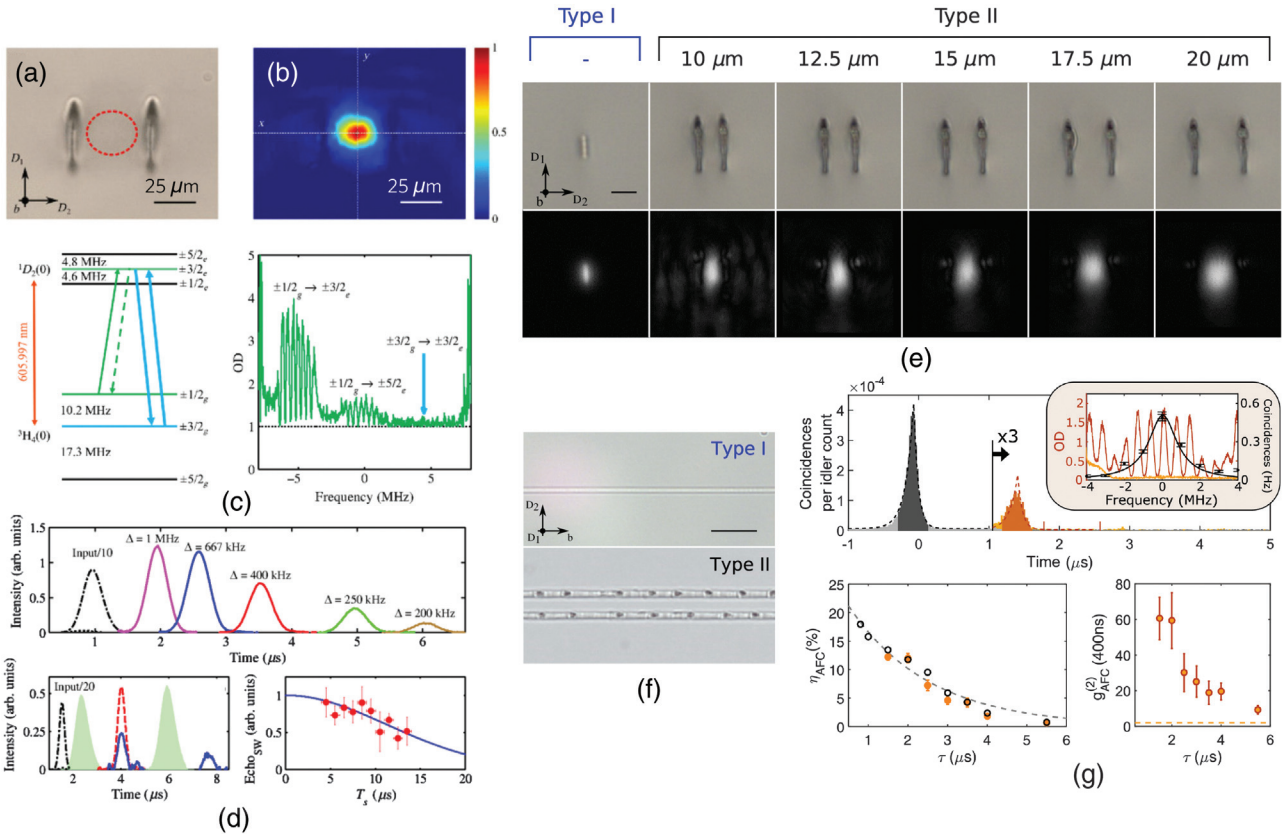

Fig. 15 (a), (b) Microscope image and near-field intensity profile of a type-II waveguide in a $Pr^{3+}:Y_2SiO_5$ crystal. (c) Energy-level structure of $^3H_4$ ground and $^1D_2$ excited manifolds. (d) Light-storage experiments using the AFC protocol. Images (a)–(d) are reproduced with permission from Ref. 229, © 2016 American Physical Society (APS). (e), (f) End-face and top-view microscope images of type I and type II waveguides and modal profiles in $Pr^{3+}:Y_2SiO_5$ crystal, respectively. (g) Time-resolved histogram for signal photons, internal storage efficiency η_{AFC} at different storage times, and cross-correlation values between idler photons and stored signal photons. Images (e)–(g) are reprinted with permission from Ref. 52, © 2018 Optica.

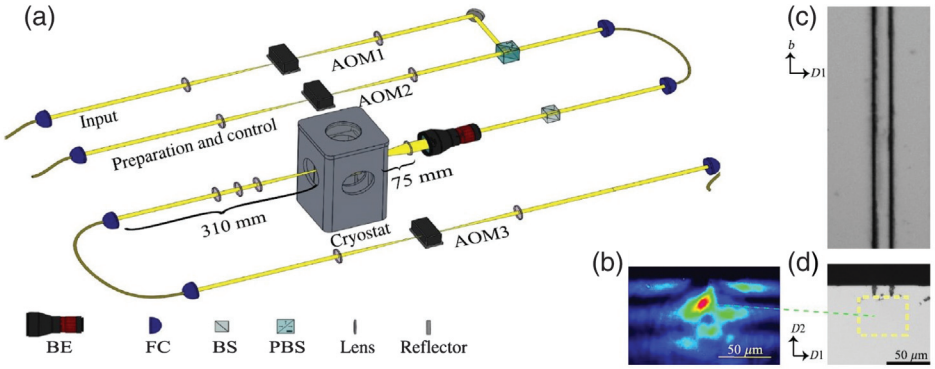

Fig. 16 (a) Experimental setup of coherent optical memory based on an on-chip waveguide. (b) Guided mode intensity distribution of laser-written ridge waveguides in an $Eu^{3+}:Y_2SiO_5$ crystal. (c), (d) Top and front view microscope images. Images are reproduced with permission from Ref. 230, © 2020 APS.

a single-mode LNOI waveguide with a propagation loss of 0.029 dB/cm at 1550 nm has also been discussed.[236] Based on these ultralow-loss waveguides, Wang et al.[237] demonstrated the fabrication of LNOI beam splitters and Mach–Zehnder interferometers. Later in 2020, Zhou et al.[236] successfully designed and fabricated optical true delay lines on the LNOI chip, realizing a relative time delay of 2.285 ns. Various waveguides with lengths from ~10 to ~100 cm have been fabricated with

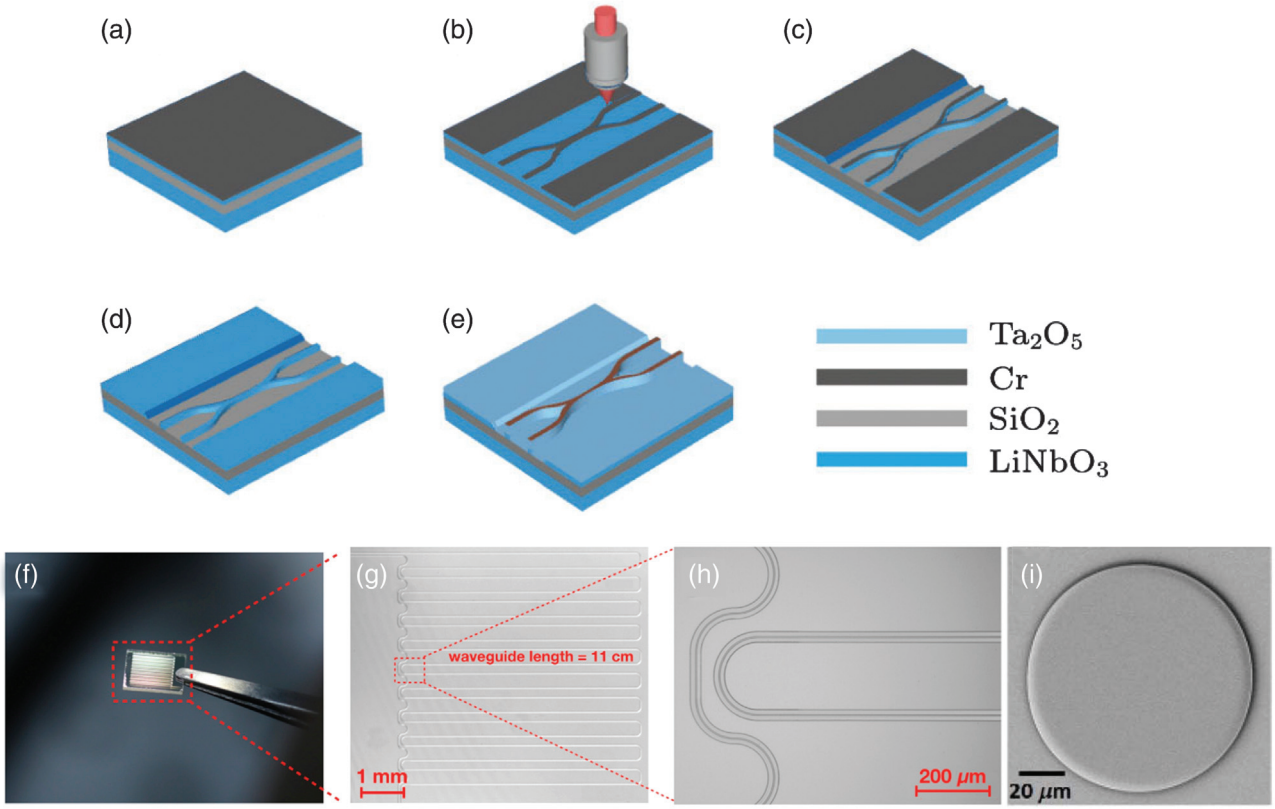

Fig. 17 Schematic illustration of the PLACE fabrication process. (a) Cr thin-film deposition, (b) Cr patterning, (c) CMP, (d) chemical wet etching, and (e) coating Ta_2O_5 film. Images (a)–(e) are reproduced with permission from Ref. 236, © 2020 Chinese Physical Society (CPL). (f) Camera photo of the 11-cm-long LNOI waveguide, (g) microscope image, and (h) enlarged image. Images (f)–(h) are reproduced with permission from Ref. 232, CC-BY. (i) SEM image of LNOI microdisk. Image (i) is reproduced with permission from Ref. 233, CC-BY.

losses below 0.03 dB/cm, providing the large-scale on-chip integration of numerous unit microdevices.

To date, some active components, such as on-chip microlasers and amplifiers, have also played an important role in the monolithic integration of PICs. In 2021, Wang et al.[238] demonstrated a tunable microring laser on Er^{3+}-doped LNOI, enabling a low threshold of 400 μW. In the same year, by integrating the microelectrodes, an electro-optically tunable microring laser has been achieved on an LNOI platform on which the laser wavelength can be tuned with an electro-optic coefficient of 0.33 pm/V.[239] Specifically, their group provided an alternative pumping manner, using an undoped LNOI waveguide directly bonded above the Er^{3+}-doped microring, rather than the tapered fibers. In addition, Zhou et al.[240] proposed an on-chip waveguide amplifier on Er^{3+}-doped LNOI, which allows a net gain of 18 dB for a length of 3.6 cm emitting of 1530 nm, indicating an efficient broadband amplification.

5 Summary and Perspectives

Femtosecond laser inscribed crystalline waveguides play increasingly significant roles in modern photonic circuits, offering an attractive platform for multifunctional integrated optical applications. The unique 3D microfabrication of femtosecond lasers is currently driving the success of new devices and functionalities, such as quantum and on-chip photonics. Recent progress and achievements in this research field are briefly overviewed, whereas a few challenges and potential topics remain to be further investigated.

First, the underlying mechanism of different refractive index modifications induced by femtosecond lasers is not entirely understood, which strongly depends on the parameters of the laser processing system and the physical properties of crystals. For example, an interesting phase transformation from YAG to YAP crystal is observed by Okhrimchuk et al.[86] under direct laser writing, relating to rapid quenching after overheated crystal melting. Future investigation towards the mechanisms of refractive index modification and the phase-change transitions is planned. Second, a severe limitation of femtosecond laser inscription is related to the relatively lower refractive index contrast than that of bulk, usually on the magnitude of 10^{-3} in crystals. Thus the miniaturization of femtosecond laser-processed photonic devices and many applications are limited. Further work will focus on the formation of waveguides with an enhanced photoinduced refractive index contrast while preserving the morphology and uniformity of laser-induced modifications. Third, waveguide-integrated photonic devices have a significant interest in large-scale on-chip circuits, thus the waveguide performances, including propagation loss, bending radii, and coupling efficiencies with other optical components, need to be

further improved via optimizing design and fabrication. Benefitting from the 3D capability of femtosecond laser writing, more complex structures are expected to improve the integration density for multifunctional devices in crystals, such as lantern waveguides,[174] high-channel interposers,[176] and helical waveguide arrays[175] that have been achieved in glass. Fourth, some femtosecond laser micromachined on-chip LNOI devices as mentioned in Sec. 4.4 are opening an avenue for scalable integrated applications. Notably, the outstanding nonlinear properties of LNOI compared with silicon on insulator will be very attractive for future PICs. Therefore, the performance of LNOI requires further investigation by carefully designed domain structures for enhancing nonlinear conversion efficiency, whereas femtosecond laser-engineered domain modification is an efficient manner. Considering a relatively large nonlinear coefficient ($d_{33} \approx 26$ pm/V), LT-on-insulator (LTOI) is another fascinating alternative for on-chip photonics who possesses a higher optical damage threshold (240 MW/cm^2) and a greater UV transparency (0.28 to 5.5 μm), whereas there is little research in LTOI devices and their nonlinear characterization.[241] Fifth, laser-written waveguides may receive wider applications in the field of quantum photonics. Most recently, using a single-mode waveguide and a doughnut-shaped waveguide fabricated by femtosecond laser direct writing, Chen et al.[48] demonstrated the vector vortex beam emitter carrying spin and orbital angular momentum mode inside a photonic chip, allowing for high-dimensional quantum information processing. Further optimizations concern the research of indistinguishable vortex photonic states and on-chip quantum interference. In addition, laser-written waveguides play an important role in single-photon sources, and QMs based on rare-earth doped waveguides, promising potential applications at the visible wavelength band. Large memory arrays and matrices in one crystal can be expected for massively multiplexed QMs in the near future.

In summary, recent advances of femtosecond laser-written waveguides in crystalline materials are overviewed. First, this review presents an introduction to the modification induced by femtosecond laser processing of dielectric crystals, including the fundamentals, control of laser-induced tracks, beam shaping techniques, waveguide geometries, and mode modulation. Track morphology engineering is crucial for not only tailoring the properties of the waveguide but also for the fabrication of novel photonic structures, such as 3D NPCs, 3D domain grating structures, nanopores, and microstructured optical waveguides. Then progress in 3D laser-written photonic devices is discussed, including 3D beam-splitters, tapered waveguides, 3D waveguide arrays, and 3D directional couplers. Last but not least, the selected applications, such as waveguide lasers, frequency converters, QMs, and on-chip devices, have been reviewed in detail. Future challenges and potential topics that could be realized in laser-written waveguides have also been proposed. Overall, it can be concluded that femtosecond laser micromachined waveguides in crystals are still rapidly developing and expected to present the possibility for truly 3D-integrated on-chip photonics in the near future.

Acknowledgments

This work was financially supported by the National Natural Science Foundation of China (Nos. 12174222 and 61775120), the Natural Science Foundation of Shandong Province (ZR2021ZD02), and Taishan Scholars Program of Shandong Province. The authors declare that they have no known competing financial interests or personal relationships that could have appeared to influence the work reported in this paper.

References

1. D. N. Nikogosyan, *Nonlinear Optical Crystals: A Complete Survey*, Springer, New York (2005).
2. A. A. Kaminskii, *Laser Crystals: Their Physics and Properties*, Springer, Heidelberg (2013).
3. P. Ferraro et al., *Ferroelectric Crystals for Photonic Applications: Including Nanoscale Fabrication and Characterization Techniques*, Springer, Heidelberg (2009).
4. J. D. Bierlein and C. B. Arweiler, "Electro-optic and dielectric properties of $KTiOPO_4$," *Appl. Phys. Lett.* **49**(15), 917–919 (1986).
5. X.-L. Wang et al., "Experimental ten-photon entanglement," *Phys. Rev. Lett.* **117**(21), 210502 (2016).
6. D. Wei et al., "Efficient nonlinear beam shaping in three-dimensional lithium niobate nonlinear photonic crystals," *Nat. Commun.* **10**, 4193 (2019).
7. Y. Jia and F. Chen, "Compact solid-state waveguide lasers operating in the pulsed regime: a review [Invited]," *Chin. Opt. Lett.* **17**(1), 012302 (2019).
8. M. Businger et al., "Optical spin-wave storage in a solid-state hybridized electron-nuclear spin ensemble," *Phys. Rev. Lett.* **124**(5), 053606 (2020).
9. V. Bharadwaj et al., "Femtosecond laser written photonic and microfluidic circuits in diamond," *J. Phys. Photonics* **1**(2), 022001 (2019).
10. M. F. Askarani et al., "Storage and reemission of heralded telecommunication-wavelength photons using a crystal waveguide," *Phys. Rev. Appl.* **11**(5), 054056 (2019).
11. T. Zhong et al., "Interfacing broadband photonic qubits to on-chip cavity-protected rare-earth ensembles," *Nat. Commun.* **8**, 14107 (2017).
12. G. Calusine et al., "Cavity-enhanced measurements of defect spins in silicon carbide," *Phys. Rev. Appl.* **6**, 014019 (2016).
13. O. Alibart et al., "Quantum photonics at telecom wavelengths based on lithium niobate waveguides," *J. Opt.* **18**(10), 104001 (2016).
14. H. Jin et al., "On-chip generation and manipulation of entangled photons based on reconfigurable lithium-niobate waveguide circuits," *Phys. Rev. Lett.* **113**(10), 103601 (2014).
15. E. Saglamyurek et al., "Broadband waveguide quantum memory for entangled photons," *Nature* **469**(7331), 512–515 (2011).
16. S. Zhu, "Meter-level optical delay line on a low-loss lithium niobate nanophotonics chip," *Chin. Phys. Lett.* **37**(8), 080102 (2020).
17. Y. Jia et al., "Ion-cut lithium niobate on insulator technology: recent advances and perspectives," *Appl. Phys. Rev.* **8**, 011307 (2021).
18. J. Lin et al., "Advances in on-chip photonic devices based on lithium niobate on insulator," *Photonics Res.* **8**(12), 1910–1936 (2020).
19. H. L. Xu and H. B. Sun, "Femtosecond laser 3D fabrication of whispering-gallery-mode microcavities," *Sci. China Phys. Mech. Astron.* **58**(11), 114202 (2015).
20. K. Okamoto, *Fundamentals of Optical Waveguides*, Academic Press (2006).
21. M. L. Calvo and V. Lakshminarayanan, *Optical Waveguides: From Theory to Applied Technologies*, CRC Press, Boca Raton, Florida (2018).
22. C. Grivas, "Optically pumped planar waveguide lasers: part II: gain media, laser systems, and applications," *Prog. Quantum Electron.* **45–46**, 3–160 (2016).
23. F. Chen and J. R. Vázquez de Aldana, "Optical waveguides in crystalline dielectric materials produced by femtosecond-laser micromachining," *Laser Photonics Rev.* **8**(2), 251–275 (2014).

24. Y. Jia et al., "Femtosecond laser direct writing of flexibly configured waveguide geometries in optical crystals: fabrication and application," *Opto-Electron. Adv.* **3**(10), 190042 (2020).
25. S. Suntsov et al., "Er:Ti:$LiNbO_3$ ridge waveguide optical amplifiers by optical grade dicing and three-side Er and Ti in-diffusion," *Appl. Phys. B* **123**(4), 118 (2017).
26. D. Kip, "Photorefractive waveguides in oxide crystals: fabrication, properties, and applications," *Appl. Phys. B* **67**(2), 131–150 (1998).
27. P. Ganguly et al., "Determination of refractive indices from the mode profiles of UV-written channel waveguides in $LiNbO_3$-crystals for optimization of writing conditions," *J. Lightwave Technol.* **27**(16), 3490–3497 (2009).
28. F. Chen, "Micro-and submicrometric waveguiding structures in optical crystals produced by ion beams for photonic applications," *Laser Photonics Rev.* **6**(5), 622–640 (2012).
29. R. R. Gattass and E. Mazur, "Femtosecond laser micromachining in transparent materials," *Nature Photonics* **2**(4), 219–225 (2008).
30. K. Sugioka and Y. Cheng, "Ultrafast lasers—reliable tools for advanced materials processing," *Light Sci. Appl.* **3**(4), e149 (2014).
31. S. Gross and M. J. Withford, "Ultrafast-laser-inscribed 3D integrated photonics: challenges and emerging applications," *Nanophotonics* **4**(3), 332–352 (2015).
32. R. Osellame et al., *Femtosecond Laser Micromachining: Photonic and Microfluidic Devices in Transparent Materials*, Springer Science & Business Media, Heidelberg, Germany (2012).
33. K. M. Davis et al., "Writing waveguides in glass with a femtosecond laser," *Opt. Lett.* **21**(21), 1729–1731 (1996).
34. D. Z. Tan et al., "Photonic circuits written by femtosecond laser in glass: improved fabrication and recent progress in photonic devices," *Adv. Photonics* **3**(2), 024002 (2021).
35. F. Sima et al., "Three-dimensional femtosecond laser processing for lab-on-a-chip applications," *Nanophotonics* **7**(3), 613–634 (2018).
36. Z. C. Ma et al., "Femtosecond-laser direct writing of metallic micro/nanostructures: from fabrication strategies to future applications," *Small Methods* **2**(7), 1700413 (2018).
37. B. Zhang et al., "Recent advances in femtosecond laser processing of $LiNbO_3$ crystals for photonic applications," *Laser Photonics Rev.* **14**(8), 1900407 (2020).
38. W. M. Pätzold et al., "Low-loss curved waveguides in polymers written with a femtosecond laser," *Opt. Express* **25**(1), 263–270 (2017).
39. Z.-Z. Li et al., "Circular cross section waveguides processed by multi-foci-shaped femtosecond pulses," *Opt. Lett.* **46**(3), 520–523 (2021).
40. Q. Zhang et al., "Single scan femtosecond laser transverse writing of depressed cladding waveguides enabled by three-dimensional focal field engineering," *Opt. Express* **25**(12), 13263–13270 (2017).
41. J. Qi et al., "Fabrication of polarization-independent single-mode waveguides in lithium niobate crystal with femtosecond laser pulses," *Opt. Mater. Express* **6**(8), 2554–2559 (2016).
42. P. Wang et al., "Fabrication of polarization-independent waveguides deeply buried in lithium niobate crystal using aberration-corrected femtosecond laser direct writing," *Sci. Rep.* **7**, 41211 (2017).
43. J. Imbrock et al., "Waveguide-integrated three-dimensional quasi-phase-matching structures," *Optica* **7**(1), 28–34 (2020).
44. J. Wang et al., "Integrated photonic quantum technologies," *Nat. Photonics* **14**(5), 273–284 (2020).
45. C.-Y. Wang et al., "On-chip rotated polarization directional coupler fabricated by femtosecond laser direct writing," *Opt. Lett.* **44**(1), 102–105 (2019).
46. H. Tang et al., "Experimental two-dimensional quantum walk on a photonic chip," *Sci. Adv.* **4**(5), eaat3174 (2018).
47. Y. Chen et al., "Mapping twisted light into and out of a photonic chip," *Phys. Rev. Lett.* **121**(23), 233602 (2018).
48. Y. Chen et al., "Vector vortex beam emitter embedded in a photonic chip," *Phys. Rev. Lett.* **124**(15), 153601 (2020).
49. S. Atzeni et al., "Integrated sources of entangled photons at the telecom wavelength in femtosecond-laser-written circuits," *Optica* **5**(3), 311–314 (2018).
50. C. Liu et al., "Reliable coherent optical memory based on a laser-written waveguide," *Optica* **7**(2), 192–197 (2020).
51. C. Liu et al., "On-demand quantum storage of photonic qubits in an on-chip waveguide," *Phys. Rev. Lett.* **125**(26), 260504 (2020).
52. A. Seri et al., "Laser-written integrated platform for quantum storage of heralded single photons," *Optica* **5**(8), 934–941 (2018).
53. A. Seri et al., "Quantum storage of frequency-multiplexed heralded single photons," *Phys. Rev. Lett.* **123**(8), 080502 (2019).
54. M. Malinauskas et al., "Ultrafast laser processing of materials: from science to industry," *Light Sci. Appl.* **5**(8), e16133 (2016).
55. E. Glezer et al., "Three-dimensional optical storage inside transparent materials," *Opt. Lett.* **21**(24), 2023–2025 (1996).
56. L. V. Keldysh, "Ionization in the field of a strong electromagnetic wave," *Sov. Phys. JETP* **20**(5), 1307–1314 (1965).
57. S. Sundaram and E. Mazur, "Inducing and probing non-thermal transitions in semiconductors using femtosecond laser pulses," *Nat. Mater.* **1**(4), 217–224 (2002).
58. C. Phipps, *Laser Ablation and Its Applications*, Springer, Heidelberg, Germany (2007).
59. N. Bloembergen, "Laser-induced electric breakdown in solids," *IEEE J. Quantum Electron.* **10**(3), 375–386 (1974).
60. K. Sugioka and Y. Cheng, *Ultrafast Laser Processing: From Micro -to Nanoscale*, CRC Press, Pan Stanford (2013).
61. S. Nolte et al., "Ablation of metals by ultrashort laser pulses," *J. Opt. Soc. Am. B* **14**(10), 2716–2722 (1997).
62. A. M. Streltsov and N. F. Borrelli, "Study of femtosecond-laser-written waveguides in glasses," *J. Opt. Soc. Am. B* **19**(10), 2496–2504 (2002).
63. J. Burghoff, S. Nolte, and A. Tünnermann, "Origins of waveguiding in femtosecond laser-structured $LiNbO_3$," *Appl. Phys. A* **89**, 127–132 (2007).
64. B. McMillen, C. Athanasiou, and Y. Bellouard, "Femtosecond laser direct-write waveplates based on stress-induced birefringence," *Opt. Express* **24**(24), 27239–27252 (2016).
65. Y. Ren et al., "Femtosecond laser irradiation on Nd:YAG crystal: surface ablation and high-spatial-frequency nanograting," *Appl. Surf. Sci.* **441**, 372–380 (2018).
66. G. Eberle et al., "Laser surface and subsurface modification of sapphire using femtosecond pulses," *Appl. Surf. Sci.* **378**, 504–512 (2016).
67. D. C. Deshpande et al., "Investigation of femtosecond laser assisted nano and microscale modifications in lithium niobate," *J. Appl. Phys.* **97**(7), 074316 (2005).
68. J. Song et al., "Formation mechanism of self-organized voids in dielectrics induced by tightly focused femtosecond laser pulses," *Appl. Phys. Lett.* **92**(9), 092904 (2008).
69. D. Tan, B. Zhang, and J. Qiu, "Ultrafast laser direct writing in glass: thermal accumulation engineering and applications," *Laser Photonics Rev.* **15**(9), 2000455 (2021).
70. M. D. Perry et al., "Ultrashort-pulse laser machining of dielectric materials," *J. Appl. Phys.* **85**(9), 6803–6810 (1999).
71. M. Lenzner et al., "Femtosecond optical breakdown in dielectrics," *Phys. Rev. Lett.* **80**(18), 4076–4079 (1998).
72. T. Jia et al., "Ultraviolet-infrared femtosecond laser-induced damage in fused silica and CaF_2 crystals," *Phys. Rev. B* **73**(5), 054105 (2006).
73. K. Itoh et al., "Ultrafast processes for bulk modification of transparent materials," *MRS Bull.* **31**(8), 620–625 (2006).
74. S. M. Eaton et al., "Heat accumulation effects in femtosecond laser-written waveguides with variable repetition rate," *Opt. Express* **13**(12), 4708–4716 (2005).

75. W. Nie et al., "Optical lattice-like cladding waveguides by direct laser writing: fabrication, luminescence, and lasing," *Opt. Lett.* **41**(10), 2169–2172 (2016).
76. D. Ashkenasi et al., "Surface damage threshold and structuring of dielectrics using femtosecond laser pulses: the role of incubation," *Appl. Surf. Sci.* **150**(1–4), 101–106 (1999).
77. A. H. Nejadmalayeri et al., "Inscription of optical waveguides in crystalline silicon by mid-infrared femtosecond laser pulses," *Opt. Lett.* **30**(9), 964–966 (2005).
78. A. Dupont et al., "From near-UV to long-wave infrared waveguides inscribed in barium fluoride using a femtosecond laser," *Opt. Lett.* **46**(16), 3925–3928 (2021).
79. T. Feng et al., "Pulse-propagation modeling and experiment for femtosecond-laser writing of waveguide in Nd:YAG," *Crystals* **9**(8), 434 (2019).
80. J.-P. Bérubé et al., "Femtosecond laser inscription of depressed cladding single-mode mid-infrared waveguides in sapphire," *Opt. Lett.* **44**(1), 37–40 (2019).
81. M. A. Butt et al., "Low-repetition rate femtosecond laser writing of optical waveguides in KTP crystals: analysis of anisotropic refractive index changes," *Opt. Express* **23**(12), 15343–15355 (2015).
82. R. Osellame et al., "Optical properties of waveguides written by a 26 MHz stretched cavity Ti:sapphire femtosecond oscillator," *Opt. Express* **13**(2), 612–620 (2005).
83. J. Burghoff et al., "Efficient frequency doubling in femtosecond laser-written waveguides in lithium niobate," *Appl. Phys. Lett.* **89**(8), 081108 (2006).
84. J. R. MacDonald et al., "Ultrafast laser inscription of near-infrared waveguides in polycrystalline ZnSe," *Opt. Lett.* **35**(23), 4036–4038 (2010).
85. A. Rodenas and A. K. Kar, "High-contrast step-index waveguides in borate nonlinear laser crystals by 3D laser writing," *Opt. Express* **19**(18), 17820–17833 (2011).
86. A. G. Okhrimchuk et al., "Phase transformation under direct laser writing in a YAG single crystal," *Opt. Mater. Express* **7**(9), 3408–3421 (2017).
87. Y. Zhang et al., "Femtosecond laser direct writing of Nd:YAG waveguide with type I modification: positive refractive index change in track," *Opt. Mater.* **113**, 110844 (2021).
88. J. Lv et al., "Three-dimensional femtosecond laser fabrication of waveguide beam splitters in $LiNbO_3$ crystal," *Opt. Mater. Express* **5**(6), 1274–1280 (2015).
89. R. He et al., "Three-dimensional dielectric crystalline waveguide beam splitters in mid-infrared band by direct femtosecond laser writing," *Opt. Express* **22**(25), 31293–31298 (2014).
90. J. Burghoff et al., "Structural properties of femtosecond laser-induced modifications in $LiNbO_3$," *Appl. Phys. A* **86**(2), 165–170 (2007).
91. B. Zhang et al., "Mode tailoring of laser written waveguides in $LiNbO_3$ crystals by multi-scan of femtosecond laser pulses," *Opt. Mater.* **86**, 571–575 (2018).
92. A. Rodenas et al., "Refractive index change mechanisms in femtosecond laser written ceramic Nd:YAG waveguides: micro-spectroscopy experiments and beam propagation calculations," *Appl. Phy. B* **95**, 85–96 (2009).
93. J. Thomas et al., "Femtosecond laser-written quasi-phase-matched waveguides in lithium niobate," *Appl. Phys. Lett.* **91**(15), 151108 (2007).
94. Y. Liao et al., "Electro-optic integration of embedded electrodes and waveguides in $LiNbO_3$ using a femtosecond laser," *Opt. Lett.* **33**(19), 2281–2283 (2008).
95. D. S. da Silva et al., "Production and characterization of femtosecond laser-written double line waveguides in heavy metal oxide glasses," *Opt. Mater.* **75**, 267–273 (2018).
96. G. A. Torchia et al., "Highly efficient laser action in femtosecond-written Nd:yttrium aluminum garnet ceramic waveguides," *Appl. Phys. Lett.* **92**(11), 111103 (2008).
97. T. Calmano et al., "Laser oscillation in Yb:YAG waveguide beam-splitters with variable splitting ratio," *Opt. Lett.* **40**(8), 1753–1756 (2015).
98. H. Liu et al., "Femtosecond laser inscribed cladding waveguides in Nd:YAG ceramics: fabrication, fluorescence imaging and laser performance," *Opt. Express* **20**(17), 18620–18629 (2012).
99. H. D. Nguyen et al., "Low-loss 3D-laser-written mid-infrared $LiNbO_3$ depressed-index cladding waveguides for both TE and TM polarizations," *Opt. Express* **25**(4), 3722–3736 (2017).
100. Y. Jia et al., "Monolithic crystalline cladding microstructures for efficient light guiding and beam manipulation in passive and active regimes," *Sci. Rep.* **4**, 5988 (2014).
101. Y. Jia et al., "Three-dimensional waveguide splitters inscribed in Nd:YAG by femtosecond laser writing: realization and laser emission," *J. Lightwave Technol.* **34**(4), 1328–1332 (2016).
102. F. Chen and J. Vázquez de Aldana, "Laser-written 3D crystalline photonic devices," *SPIE News*, 24 July 2015, https://spie.org/news/6006-laser-written-3d-crystalline-photonic-devices (accessed March 2022).
103. J. Lapointe et al., "Nonlinear increase, invisibility, and sign inversion of a localized fs-laser-induced refractive index change in crystals and glasses," *Light Sci. Appl.* **9**, 64 (2020).
104. V. Lucarini et al., *Kramers-Kronig Relations in Optical Materials Research*, Springer Science & Business Media (2005).
105. K. Miura et al., "Photowritten optical waveguides in various glasses with ultrashort pulse laser," *Appl. Phys. Lett.* **71**(23), 3329–3331 (1997).
106. C. Hnatovsky et al., "Pulse duration dependence of femtosecond-laser-fabricated nanogratings in fused silica," *Appl. Phys. Lett.* **87**, 014104 (2005).
107. S. Juodkazis et al., "Laser-induced microexplosion confined in the bulk of a sapphire crystal: evidence of multimegabar pressures," *Phys. Rev. Lett.* **96**(16), 166101 (2006).
108. J. E. Greivenkamp, *Field Guide to Geometrical Optics*, SPIE Press, Bellingham, Washington (2004).
109. L. Li et al., "Femtosecond laser writing of optical waveguides by self-induced multiple refocusing in $LiTaO_3$ crystal," *J. Lightwave Technol.* **37**(14), 3452–3458 (2019).
110. Z. Wu et al., "Multiple foci and a long filament observed with focused femtosecond pulse propagation in fused silica," *Opt. Lett.* **27**(6), 448–450 (2002).
111. E. Toratani, M. Kamata, and M. Obara, "Self-fabrication of void array in fused silica by femtosecond laser processing," *Appl. Phys. Lett.* **87**(17), 171103 (2005).
112. R. W. Boyd. *Nonlinear Optics*, Academic, New York (2003).
113. A. Rodenas et al., "Confocal Raman imaging of optical waveguides in $LiNbO_3$ fabricated by ultrafast high-repetition rate laser-writing," *Opt. Express* **16**(18), 13979–13989 (2008).
114. J. W. Chan et al., "Waveguide fabrication in phosphate glasses using femtosecond laser pulses," *Appl. Phys. Lett.* **82**(15), 2371–2373 (2003).
115. G. R. Castillo et al., "Stress-induced waveguides in Nd:YAG by simultaneous double-beam irradiation with femtosecond pulses," *Opt. Mater.* **51**, 84–88 (2016).
116. G. Cerullo et al., "Femtosecond micromachining of symmetric waveguides at 1.5 μm by astigmatic beam focusing," *Opt. Lett.* **27**(21), 1938–1940 (2002).
117. V. Garzillo et al., "Optimization of laser energy deposition for single-shot high aspect-ratio microstructuring of thick BK7 glass," *J. Appl. Phys.* **120**, 013102 (2016).
118. Q. Zhang et al., "Reconfigurable directional coupler in lithium niobate crystal fabricated by three-dimensional femtosecond laser focal field engineering," *Photonics Res.* **7**(5), 503–507 (2019).
119. J. Thomas et al., "Quasi-phase matching in femtosecond pulse volume structured x-cut lithium niobate," *Laser Photonics Rev.* **7**(3), L17–L20 (2013).

120. L. M. Mazur et al., "Localized ferroelectric domains via laser poling in monodomain calcium barium niobate crystal," *Laser Photonics Rev.* **15**(9), 2100088 (2021).
121. D. Wei et al., "Experimental demonstration of a three-dimensional lithium niobate nonlinear photonic crystal," *Nat. Photonics* **12**(10), 596–600 (2018).
122. S. Liu et al., "Nonlinear volume holography in 3D nonlinear photonic crystals," *Laser Photonics Rev.* **14**(11), 2000224 (2020).
123. P. Chen et al., "Quasi-phase-matching-division multiplexing holography in a three-dimensional nonlinear photonic crystal," *Light Sci. Appl.* **10**, 146 (2021).
124. M. Shao et al., "Pushing periodic-disorder-induced phase matching into the deep-ultraviolet spectral region: theory and demonstration," *Light Sci. Appl.* **9**, 45 (2020).
125. T. Xu et al., "Three-dimensional nonlinear photonic crystal in ferroelectric barium calcium titanate," *Nat. Photonics* **12**(10), 591–595 (2018).
126. X. Chen et al., "Quasi-phase matching via femtosecond laser-induced domain inversion in lithium niobate waveguides," *Opt. Lett.* **41**(11), 2410–2413 (2016).
127. S. Kroesen et al., "Monolithic fabrication of quasi-phase-matched waveguides by femtosecond laser structuring the $\chi^{(2)}$ nonlinearity," *Appl. Phys. Lett.* **107**(10), 101109 (2015).
128. S. Kiyama et al., "Examination of etching agent and etching mechanism on femotosecond laser microfabrication of channels inside vitreous silica substrates," *Phys. Chem. C* **113**(27), 11560–11566 (2009).
129. J. Lv et al., "Mid-infrared waveguiding in three-dimensional microstructured optical waveguides fabricated by femtosecond-laser writing and phosphoric acid etching," *Photonics Res.* **8**(3), 257–262 (2020).
130. D. Choudhury et al., "Three-dimensional microstructuring of yttrium aluminum garnet crystals for laser active optofluidic applications," *Appl. Phys. Lett.* **103**(4), 041101 (2013).
131. A. Ródenas et al., "Three-dimensional femtosecond laser nanolithography of crystals," *Nat. Photonics* **13**(2), 105–109 (2019).
132. P. Wu et al., "Annular waveguide lasers at 1064 nm in Nd:YAG crystal produced by femtosecond laser inscription," *Appl. Opt.* **57**(19), 5420–5424 (2018).
133. H. Liu et al., "Waveguiding microstructures in Nd:YAG with cladding and inner dual-line configuration produced by femtosecond laser inscription," *Opt. Mater.* **39**, 125–129 (2015).
134. C. Zhang et al., "Channel waveguide lasers in Nd:GGG crystals fabricated by femtosecond laser inscription," *Opt. Express* **19**(13), 12503–12508 (2011).
135. H. Liu et al., "Continuous wave laser operation in Nd:GGG depressed tubular cladding waveguides produced by inscription of femtosecond laser pulses," *Opt. Mater. Express* **3**(2), 278–283 (2013).
136. L. Li et al., "Laser-writing of ring-shaped waveguides in BGO crystal for telecommunication band," *Opt. Express* **25**(20), 24236–24241 (2017).
137. R. He et al., "Femtosecond-laser micromachined optical waveguides in $Bi_4Ge_3O_{12}$ crystals," *Appl. Opt.* **52**(16), 3713–3718 (2013).
138. W. Silva et al., "Femtosecond-laser-written, stress-induced Nd:YVO_4 waveguides preserving fluorescence and Raman gain," *Opt. Lett.* **35**(7), 916–918 (2010).
139. G. Salamu and N. Pavel, "Power scaling from buried depressed-cladding waveguides realized in Nd:YVO_4 by femtosecond-laser beam writing," *Opt. Laser Technol.* **84**, 149–154 (2016).
140. Z. Li et al., "Near-infrared all-optical switching based on nano/micro optical structures in YVO_4 matrix: embedded plasmonic nanoparticles and laser-written waveguides," *Adv. Photonics Res.* **2**(1), 2000064 (2021).
141. Y. Tan et al., "70% slope efficiency from an ultrafast laser-written Nd:$GdVO_4$ channel waveguide laser," *Opt. Express* **18**(24), 24994–24999 (2010).
142. H. Liu et al., "Efficient laser emission from cladding waveguide inscribed in Nd:$GdVO_4$ crystal by direct femtosecond laser writing," *Opt. Lett.* **39**(15), 4553–4556 (2014).
143. B. Zhang et al., "Femtosecond laser modification of 6H–SiC crystals for waveguide devices," *Appl. Phys. Lett.* **116**(11), 111903 (2020).
144. J. Lv et al., "Green up-conversion and near-infrared luminescence of femtosecond-laser-written waveguides in Er^{3+}, MgO co-doped nearly stoichiometric $LiNbO_3$ crystal," *Opt. Express* **24**(22), 25482–25490 (2016).
145. J. Lv et al., "Femtosecond laser writing of optical-lattice-like cladding structures for three-dimensional waveguide beam splitters in $LiNbO_3$ crystal," *J. Lightwave Technol.* **34**(15), 3587–3591 (2016).
146. L. Li et al., "All-laser-micromachining of ridge waveguides in $LiNbO_3$ crystal for mid-infrared band applications," *Sci. Rep.* **7**, 7034 (2017).
147. B. Wu et al., "Recoverable and rewritable waveguide beam splitters fabricated by tailored femtosecond laser writing of lithium tantalate crystal," *Opt. Laser Technol.* **145**, 107500 (2022).
148. L. Li et al., "Efficient quasi-phase-matching in fan-out PPSLT crystal waveguides by femtosecond laser direct writing," *Opt. Express* **27**(25), 36875–36885 (2019).
149. C. Cheng et al., "Superficial waveguide splitters fabricated by femtosecond laser writing of $LiTaO_3$ crystal," *Opt. Eng.* **54**(6), 067113 (2015).
150. Z. Li et al., "Low-loss optical waveguides in β-BBO crystal fabricated by femtosecond-laser writing," *Opt. Mater.* **73**, 45–49 (2017).
151. V. Apostolopoulos et al., "Femtosecond-irradiation-induced refractive-index changes and channel waveguiding in bulk Ti^{3+}:sapphire," *Appl. Phys. Lett.* **85**(7), 1122–1124 (2004).
152. C. Grivas et al., "Generation of multi-gigahertz trains of phase-coherent femtosecond laser pulses in Ti:sapphire waveguides," *Laser Photonics Rev.* **12**(11), 1800167 (2018).
153. Y. Ren et al., "Optical-lattice-like waveguide structures in Ti:sapphire by femtosecond laser inscription for beam splitting," *Opt. Mater. Express* **7**(6), 1942–1949 (2017).
154. S. Campbell et al., "Frequency-doubling in femtosecond laser inscribed periodically-poled potassium titanyl phosphate waveguides," *Opt. Express* **15**(25), 17146–17150 (2007).
155. F. Laurell et al., "Laser-written waveguides in KTP for broadband type II second harmonic generation," *Opt. Express* **20**(20), 22308–22313 (2012).
156. N. Dong et al., "Efficient second harmonic generation by birefringent phase matching in femtosecond-laser-inscribed KTP cladding waveguides," *Phys. Status Solid-RRL* **6**(7), 306–308 (2012).
157. W. Nie et al., "Efficient second harmonic generation in 3D nonlinear optical-lattice-like cladding waveguide splitters by femtosecond laser inscription," *Sci. Rep.* **6**, 22310 (2016).
158. W. Nie et al., "Dual-wavelength waveguide lasers at 1064 and 1079 nm in Nd:YAP crystal by direct femtosecond laser writing," *Opt. Lett.* **40**(10), 2437–2440 (2015).
159. L. Li et al., "Femtosecond-laser-written S-curved waveguide in Nd:YAP crystal: fabrication and multi-gigahertz lasing," *J. Lightwave Technol.* **38**(24), 6845–6852 (2020).
160. Y. Jia et al., "Femtosecond-laser-inscribed BiB_3O_6 nonlinear cladding waveguide for second-harmonic generation," *Appl. Phys. Express* **5**(7), 072701 (2012).
161. Y. Ren et al., "Near-infrared lasers and self-frequency-doubling in Nd:YCOB cladding waveguides," *Opt. Express* **21**(9), 11562–11567 (2013).
162. Y. Jia et al., "Enhanced second harmonic generation in femtosecond laser inscribed double-cladding waveguide of Nd:GdCOB crystal," *J. Lightwave Technol.* **31**(23), 3873–3878 (2013).
163. H. Liu et al., "Continuous-wave lasing at 1.06 μm in femtosecond laser written Nd:KGW waveguides," *Opt. Mater.* **37**, 93–96 (2014).

164. S. Li et al., "Cladding waveguide lasers in femtosecond laser written Nd:KGW waveguides," *Opt. Mater.* **110**, 110517 (2020).
165. Y. Ren et al., "Ti:sapphire micro-structures by femtosecond laser inscription: guiding and luminescence properties," *Opt. Mater.* **58**, 61–66 (2016).
166. E. Kifle et al., "Watt-level ultrafast laser inscribed thulium waveguide lasers," *Prog. Quantum. Electron.* **72**, 100266 (2020).
167. B. Wu et al., "3D polarization-dependent waveguide arrays in $LiNbO_3$ crystal produced by femtosecond laser writing," *J. Lightwave Technol.* **38**(15), 3988–3993 (2020).
168. X. Sun et al., "Femtosecond laser direct writing of depressed cladding waveguides in Nd:YAG with "ear-like" structures: fabrication and laser generation," *Opt. Express* **29**(3), 4296–4307 (2021).
169. Y. Jia et al., "Femtosecond laser direct writing of few-mode depressed-cladding waveguide lasers," *Opt. Express* **27**(21), 30941–30951 (2019).
170. H. Liu et al., "Femtosecond laser direct writing of evanescently-coupled planar waveguide laser arrays," *Opt. Mater. Express* **9**(11), 4447–4455 (2019).
171. A. Okhrimchuk et al., "Low loss depressed cladding waveguide inscribed in YAG:Nd single crystal by femtosecond laser pulses," *Opt. Express* **20**(4), 3832–3843 (2012).
172. H. Liu et al., "Femtosecond-laser inscribed double-cladding waveguides in Nd:YAG crystal: a promising prototype for integrated lasers," *Opt. Lett.* **38**(17), 3294–3297 (2013).
173. J. R. Vázquez de Aldana et al., "Femtosecond laser direct inscription of 3D photonic devices in Er/Yb-doped oxyfluoride nano-glass ceramics," *Opt. Mater. Express* **10**(10), 2695–2704 (2020).
174. G. Douglass et al., "Novel concept for visible and near infrared spectro-interferometry: laser-written layered arrayed waveguide gratings," *Opt. Express* **26**(14), 18470–18479 (2018).
175. M. C. Rechtsman et al., "Photonic Floquet topological insulators," *Nature* **496**(7444), 196–200 (2013).
176. G. Djogo et al., "Femtosecond laser additive and subtractive micro-processing: enabling a high-channel-density silica interposer for multicore fibre to silicon-photonic packaging," *Int. J. Extrem. Manuf.* **1**(4), 045002 (2019).
177. J. Guan et al., "Component-wise testing of laser-written integrated coupled-mode beam splitters," *Opt. Lett.* **44**(12), 3174–3177 (2019).
178. A. Courvoisier et al., "Inscription of 3D waveguides in diamond using an ultrafast laser," *Appl. Phys. Lett.* **109**(3), 031109 (2016).
179. J. G. Ajates et al., "Y-junctions based on circular depressed-cladding waveguides fabricated with femtosecond pulses in Nd:YAG crystal: a route to integrate complex photonic circuits in crystals," *Opt. Mater.* **72**, 220–225 (2017).
180. H. Liu et al., "Femtosecond laser inscribed Y-branch waveguide in Nd:YAG crystal: fabrication and continuous-wave lasing," *IEEE J. Sel. Top. Quant.* **22**(2), 227–230 (2015).
181. Y. Ren et al., "Cladding waveguide splitters fabricated by femtosecond laser inscription in Ti:sapphire crystal," *Opt. Laser Technol.* **103**, 82–88 (2018).
182. J. G. Ajates et al., "Three-dimensional beam-splitting transitions and numerical modelling of direct-laser-written near-infrared $LiNbO_3$ cladding waveguides," *Opt. Mater. Express* **8**(7), 1890–1901 (2018).
183. W. Nie et al., "Implementation of nearly single-mode second harmonic generation by using a femtosecond laser written waveguiding structure in $KTiOPO_4$ nonlinear crystal," *Opt. Mater.* **84**, 531–535 (2018).
184. B. Zhang et al., "Femtosecond laser inscribed novel polarization beam splitters based on tailored waveguide configurations," *J. Lightwave Technol.* **39**(5), 1438–1443 (2020).
185. C. Romero et al., "Fabrication of tapered circular depressed-cladding waveguides in Nd:YAG crystal by femtosecond-laser direct inscription," *Micromachines* **11**(1), 10 (2020).
186. G. R. Castillo et al., "Depressed-cladding 3-D waveguide arrays fabricated with femtosecond laser pulses," *J. Lightwave Technol.* **35**(13), 2520–2525 (2017).
187. N. Skryabin et al., "Femtosecond laser written depressed-cladding waveguide 2×2, 1×2 and 3×3 directional couplers in Tm^{3+}:YAG crystal," *Micromachines* **11**(1), 1 (2020).
188. N. Dong et al., "Self-frequency-doubling of ultrafast laser inscribed neodymium doped yttrium aluminum borate waveguides," *Appl. Phys. Lett.* **98**(18), 181103 (2011).
189. T. Calmano et al., "Crystalline Pr:$SrAl_{12}O_{19}$ waveguide laser in the visible spectral region," *Opt. Lett.* **36**(23), 4620–4622 (2011).
190. F. Reichert et al., "Efficient visible laser operation of Pr, Mg:$SrAl_{12}O_{19}$ channel waveguides," *Opt. Lett.* **38**(15), 2698–2701 (2013).
191. S. Müller et al., "Femtosecond-laser-written diode-pumped Pr:$LiYF_4$ waveguide laser," *Opt. Lett.* **37**(24), 5223–5225 (2012).
192. C. Grivas et al., "Tunable, continuous-wave Ti:sapphire channel waveguide lasers written by femtosecond and picosecond laser pulses," *Opt. Lett.* **37**(22), 4630–4632 (2012).
193. Y. Ren et al., "Switchable single-dual-wavelength Yb, Na:CaF_2 waveguide lasers operating in continuous-wave and pulsed regimes," *Opt. Mater. Express* **8**(6), 1633–1641 (2018).
194. T. Calmano et al., "Curved Yb:YAG waveguide lasers, fabricated by femtosecond laser inscription," *Opt. Express* **21**(21), 25501–25508 (2013).
195. S. Hakobyan et al., "Highly efficient Q-switched Yb:YAG channel waveguide laser with 5.6 W of average output power," *Opt. Lett.* **41**(20), 4715–4718 (2016).
196. S. Y. Choi et al., "2-GHz carbon nanotube mode-locked Yb:YAG channel waveguide laser," *Opt. Express* **26**(5), 5140–5145 (2018).
197. J. E. Bae et al., "Carbon nanotube Q-switched Yb:KLuW surface channel waveguide lasers," *Opt. Lett.* **45**(1), 216–219 (2020).
198. C. Cheng et al., "Tin diselenide as a new saturable absorber for generation of laser pulses at 1 μm," *Opt. Express* **25**(6), 6132–6140 (2017).
199. Z. Li et al., "8.8 GHz Q-switched mode-locked waveguide lasers modulated by $PtSe_2$ saturable absorber," *Opt. Express* **27**(6), 8727–8737 (2019).
200. M. V. Ponarina et al., "Dual-wavelength generation of picosecond pulses with 9.8 GHz repetition rate in Nd:YAG waveguide laser with graphene," *Quantum Electron.* **49**(4), 365 (2019).
201. Z. Li et al., "Q-switching of waveguide lasers based on graphene/WS_2 van der Waals heterostructure," *Photonics Res.* **5**(5), 406–410 (2017).
202. Z. Li et al., "6.5 GHz Q-switched mode-locked waveguide lasers based on two-dimensional materials as saturable absorbers," *Opt. Express* **26**(9), 11321–11330 (2018).
203. Z. Li et al., "Mode-locked waveguide lasers modulated by rhenium diselenide as a new saturable absorber," *APL Photonics* **3**(8), 080802 (2018).
204. Y. Ren et al., "Continuous wave channel waveguide lasers in Nd:$LuVO_4$ fabricated by direct femtosecond laser writing," *Opt. Express* **20**(3), 1969–1974 (2012).
205. E. Kifle et al., "Passively Q-switched femtosecond-laser-written thulium waveguide laser based on evanescent field interaction with carbon nanotubes," *Photonics Res.* **6**(10), 971–980 (2018).
206. E. Kifle et al., "Fs-laser-written thulium waveguide lasers Q-switched by graphene and MoS_2," *Opt. Express* **27**(6), 8745–8755 (2019).
207. E. Kifle et al., "Femtosecond-laser-written Tm:$KLu(WO_4)_2$ waveguide lasers," *Opt. Lett.* **42**(6), 1169–1172 (2017).
208. E. Kifle et al., "Ultrafast laser inscription and ~2 μm laser operation of Y-branch splitters in monoclinic crystals," *J. Lightwave Technol.* **38**(16), 4374–4384 (2020).
209. Y. Ren et al., "7.8-GHz graphene-based 2-μm monolithic waveguide laser," *IEEE J. Sel. Top. Quant.* **21**(1), 395–400 (2014).
210. E. Kifle et al., "Femtosecond-laser-written Ho:$KGd(WO_4)_2$ waveguide laser at 2.1 μm," *Opt. Lett.* **44**(7), 1738–1741 (2019).

211. E. Kifle et al., "Low-loss fs-laser-written surface waveguide lasers at >2 μm in monoclinic $Tm^{3+}:MgWO_4$," *Opt. Lett.* **45**(14), 4060–4063 (2020).
212. F. Thorburn et al., "5.9 GHz graphene based *Q*-switched mode-locked mid-infrared monolithic waveguide laser," *Opt. Express* **25**(21), 26166–26174 (2017).
213. S. McDaniel et al., "Operation of Ho:YAG ultrafast laser inscribed waveguide lasers," *Appl. Opt.* **56**(12), 3251–3256 (2017).
214. J. R. Macdonald et al., "Compact Cr:ZnS channel waveguide laser operating at 2333 nm," *Opt. Express* **22**(6), 7052–7057 (2014).
215. S. A. McDaniel et al., "Power scaling of ultrafast laser inscribed waveguide lasers in chromium and iron doped zinc selenide," *Opt. Express* **24**(4), 3502–3512 (2016).
216. J. E. Bae et al., "Controllable dynamic single- and dual-channel graphene *Q*-switching in a beam-splitter-type channel waveguide laser," *Laser Photonics Rev.* **16**, 2100501 (2022).
217. J. Burghoff et al., "Waveguides in lithium niobate fabricated by focused ultrashort laser pulses," *Appl. Surf. Sci.* **253**(19), 7899–7902 (2007).
218. B. Zhang et al., "Second harmonic generation in femtosecond laser written lithium niobate waveguides based on birefringent phase matching," *Opt. Mater.* **107**, 110075 (2020).
219. Y. Jia et al., "Second harmonic generation of violet light in femtosecond-laser-inscribed BiB_3O_6 cladding waveguides," *Opt. Mater. Express* **3**(9), 1279–1284 (2013).
220. M. Triplett et al., "Multi-watt, broadband second-harmonic-generation in MgO:PPSLT waveguides fabricated with femtosecond laser micromachining," *Opt. Express* **27**(15), 21102–21115 (2019).
221. L. Li et al., "Tunable violet radiation in a quasi-phase-matched periodically poled stoichiometric lithium tantalate waveguide by direct femtosecond laser writing," *Results Phys.* **19**, 103373 (2020).
222. S. Müller et al., "Highly efficient continuous wave blue second-harmonic generation in fs-laser written periodically poled $Rb:KTiOPO_4$ waveguides," *Opt. Lett.* **39**(5), 1274–1277 (2014).
223. S. Bhardwaj et al., "Inscription of type I and depressed cladding waveguides in lithium niobate using a femtosecond laser," *Appl. Opt.* **56**(20), 5692–5697 (2017).
224. L. Wang et al., "Second harmonic generation of femtosecond laser written depressed cladding waveguides in periodically poled $MgO:LiTaO_3$ crystal," *Opt. Express* **27**(3), 2101–2111 (2019).
225. T. Meany et al., "Laser written circuits for quantum photonics," *Laser Photonics Rev.* **9**(4), 363–384 (2015).
226. G. D. Marshall et al., "Laser written waveguide photonic quantum circuits," *Opt. Express* **17**(15), 12546–12554 (2009).
227. M. Zhong et al., "Optically addressable nuclear spins in a solid with a six-hour coherence time," *Nature* **517**(7533), 177–180 (2015).
228. T. Zhong et al., "Nanophotonic rare-earth quantum memory with optically controlled retrieval," *Science* **357**(6358), 1392–1395 (2017).
229. G. Corrielli et al., "Integrated optical memory based on laser-written waveguides," *Phys. Rev. Appl.* **5**(5), 054013 (2016).
230. T.-X. Zhu et al., "Coherent optical memory based on a laser-written on-chip waveguide," *Phys. Rev. Appl.* **14**(5), 054071 (2020).
231. A. Boes et al., "Status and potential of lithium niobate on insulator (LNOI) for photonic integrated circuits," *Laser Photonics Rev.* **12**(4), 1700256 (2018).
232. R. Wu et al., "Long low-loss-litium niobate on insulator waveguides with sub-nanometer surface roughness," *Nanomaterials* **8**(11), 910 (2018).
233. J. Zhang et al., "Fabrication of crystalline microresonators of high quality factors with a controllable wedge angle on lithium niobate on insulator," *Nanomaterials* **9**(9), 1218 (2019).
234. J. Lin et al., "Fabrication of high-*Q* lithium niobate microresonators using femtosecond laser micromachining," *Sci. Rep.* **5**, 8072 (2015).
235. R. Wu et al., "Lithium niobate micro-disk resonators of quality factors above 107," *Opt. Lett.* **43**(17), 4116–4119 (2018).
236. J. Zhou et al., "Electro-optically switchable optical true delay lines of meter-scale lengths fabricated on lithium niobate on insulator using photolithography assisted chemo-mechanical etching," *Chin. Phys. Lett.* **37**(8), 084201 (2020).
237. M. Wang et al., "Chemo-mechanical polish lithography: a pathway to low loss large-scale photonic integration on lithium niobate on insulator," *Quantum Eng.* **1**(1), e9 (2019).
238. Z. Wang et al., "On-chip tunable microdisk laser fabricated on Er^{3+}-doped lithium niobate on insulator," *Opt. Lett.* **46**(2), 380–383 (2021).
239. D. Yin et al., "Electro-optically tunable microring laser monolithically integrated on lithium niobate on insulator," *Opt. Lett.* **46**(9), 2127–2130 (2021).
240. J. Zhou et al., "On-chip integrated waveguide amplifiers on erbium-doped thin-film lithium niobate on insulator," *Laser Photonics Rev.* **15**(8), 2100030 (2021).
241. X. Yan et al., "High optical damage threshold on-chip lithium tantalate microdisk resonator," *Opt. Lett.* **45**(15), 4100–4103 (2020).

Lingqi Li received her PhD from Shandong University, Jinan, China, in 2021. She is an assistant professor at the College of Physics Science of Qingdao University. From 2019 to 2020, she was a joint PhD student for a research at the Max Born Institute for Nonlinear Optics and Short-Pulse Spectroscopy. Her current research interests include femtosecond laser micro- and nanofabrication, waveguide lasers, nonlinear optics, interaction of intense femtosecond laser pulses with materials, and femtosecond pulse characterization.

Weijin Kong received his PhD from Shanghai Institute of Optics and Fine Mechanics, Chinese Academy of Sciences, in 2006. He is currently a professor at the College of Physics Science, Qingdao University, China. His research interests include micro-nano optics, waveguide laser, diffraction optics, and thin film optics.

Feng Chen received his PhD from Shandong University in 2002. He is currently a distinguished professor at the School of Physics of Shandong University. From 2003 to 2005, he was at the Clausthal University of Technology, Clausthal-Zellerfeld, Germany, as an Alexander von Humboldt research fellow. In 2006, he became a professor at Shandong University. His research interests include material modifications by ultrafast lasers and ion beams, optical waveguides, 2D materials, plasmonics, nonlinear optics, and lasers. He is a fellow of the Institute of Physics, OPTICA (formerly OSA), and SPIE, and a director board member of Chinese Physical Society. He serves as the executive editor-in-chief of *Chinese Optics Letters*, associate editor of *Optical Engineering*, and an editorial board member of *Scientific Reports*.